CONTENTS

MORPHOLOGICAL STRUCTURE STUDY AND CHEMICAL COMPOSITION OF SOLID AEROSOLS RELATED TO FAISALABAD ENVIRONMENT

M. A. K. SHAHID, K. HUSSAIN AND M. S. AWAN

Department of Physics, GC University, Faisalabad, Pakistan
E-mail Addresses: profkhan786@yahoo.com

ABSTRACT: Five sites of special scientific interest from Faisalabad environment with different topographical, industrial and transportational conditions were selected for the collection of solid aerosols using high volume sampler. Filtered samples were analyzed by Scanning Electron Microscope (SEM) for their morphology, X-ray Powder Diffraction (XRPD) for their compound phase analysis and Atomic Absorption Spectrophotometer (AAS) for their elemental composition. The studies illustrate how individual particle morphology and chemical analysis can be used to identify sources and complements the source attribution studies. Five important observations have been made from this study;

1. Concentration of both fine and coarse particles is strongly influenced by transportational set up and traffic density.

2. Composition of solid aerosols is also prescribed by industrial activities.

3. The coarse particles are naturally originated from soil and associated with high wind speed.

4. Carbonaceous material in various forms is ubiquitous as predicted, although identifying probable sources is a difficult task.

5. Solid aerosols are found to be in aggregated forms of smaller components (regular, irregular both).

Maximum solid aerosols were within range (0.5-10 µm) (66.61%) and minimum in the range (>10 – 93.3 µm) (33.39%). The relationship between man-made anthropogenic activities with solid aerosols was confirmed. Morphological structure study showed the complexity and stability of Faisalabad environment.

Keywords: Aerosols, Atmospheric Pollution, Morphology, Chemical composition, Size distribution, Complexity of Faisalabad environment.

1. INTRODUCTION

Solid aerosols are a complex mixture of organic and inorganic substances, suspended in the atmosphere as both liquids and solids, and they vary in size from a few nm in diameter to 100 or more µm. They also vary in their physical and chemical properties like shape, texture, chemical composition etc. The size of solid aerosols is responsible for their transport and removal from the air, their deposition within the respiratory system. It is also associated with their chemical composition and sources.

They are generally distinguished as fine (<2.5 µm) particles, ultrafine (<0.1 µm) particles and coarse (>2.5 µm) particles. The fine particles grow from the gas phase by agglomeration. These are generally man-made having secondary origin and consist of sulfate, ammonium and nitrate ions, elemental carbon, organic carbon compounds, water and small amount of soil dust, and trace species (Pb, Cd, V, Ni, Cu, Zn, Mn, Fe etc.). These can remain suspended in air from days to weeks, can

travel hundreds to greater than thousands km and strongly associated with decreased visibility (haze). On the other hand coarse particles are of primary nature and thus originated by mechanical forces such as crushing, grinding and abrasion of materials of geological origin. Pollen and spores also lie in this range. Normally these particles consist of aluminosilicate and other oxides of crystal elements. Their key sources include fugitive dust from roads, industry, agriculture, construction and demolition, and fossil fuel combustion. These can suspend in air from minutes to hours and can travel from less than 1 km to 10km.

The main natural source of airborne particulates is sea spray and soil re-suspension by the wind and atmospheric turbulence, Saharan dust and volcano storms. These result in the natural background concentration that varies according to local sources or specific weather conditions. In most European countries, industrialization results in anthropogenic sources predomination especially in urban areas. The most significant of these are traffic, power plants, combustion sources (industrial and residential), industrial fugitive dust, loading/ unloading of bulk goods, mining activities, human started forest fires and, non-combustion sources such as building construction and quarrying. The same is true in case of our experimental findings [1].

The effect of solid aerosols on human health is strongly dependent on their capability to penetrate into the respiratory tract. Smaller particles penetrate into the respiratory system more deeply. Coarse particles may be deposited into the pharynx and larynx, causing dryness of the nose and throat having no effect on the mucociliary clearance. Environmental Protection Agency is emphasizing on developing air quality standards based on the specific size of solid aerosols, which can reach the trachea [2]. For this purpose a cut-off of 10-15 µm diameters has been proposed for inhalable particles [3]. Mostly a diameter of 10 µm is considered to be a boundary between suspended and depositable matter [4-5].

Morphology of the solid aerosols helps in characterizing them. Scanning electron microscope (SEM) is used to examine the samples due to limitations of optical microscope. SEM shows the shape and surface of even large particles better than the polarizing microscope, which is due to the superior depth of field and better contrast. Another advantage of the SEM is superior magnification and resolution and if electron probe micro-analyser (EPMA) is attached, it may also determine chemical composition of even tiny single particles. The present study is about morphological structure study of solid aerosols related to Faisalabad environment [6-10].

Current studies have shown that emission of natural origin exceeds 4 to 5 times than

the emission from anthropogenic sources in global scale [3]; however according to some studies [4], emission from anthropogenic sources will, up to 2040, reach the level of the natural emission mainly as a consequence of fossil fuel combustion with high increase rate in China and India. Same is true for Faisalabad, which demands specific protective measures on emergency basis.

2.   EXPERIMENTAL PROCEDURES

2.1.   MATERIALS AND METHODS

The solid aerosols were collected from randomly selected sites related to Faisalabad environment, the third largest and industrial city of Pakistan on Watman Micro fiber Glass Filter Paper (203 X 254 mm^2) using Kimoto High Volume Air Sampler with (1.13 m^3/min) sampling rate. Sampling was carried out on sunny days at temperature (28 to42) degree centigrade, relative humidity (50 - 80) % under study stream conditions (0.5 - 1) m /s wind velocity. During which wind reaches the sampler from varying directions. The sampling was carried out on 24 hour basis. Samples were examined in Scanning Electron Microscope JEOL – 1010 at National Institute for Biology and Genetic Engineering (NIBGE) Faisalabad.

Micrographs were taken at various magnifications. Sieve method and Hydrometer method were used for additional help to the Ferret's and Martin statistical method for size determination of solid aerosols [11 - 18]. For morphological structure study grid method was used [19-21]. X-ray Diffractometer (XRD) and Atomic absorption spectroscopy (AAS) were also used to supplement our results. For XRD an automated powder x-ray diffractometer (Rigaku model D/MAX-II A) was used while AAS was performed using Atomic Absorption Spectrophotometer (Varian 1475ABD) under controlled conditions.

3.   RESULTS AND DISCUSSION

3.1   SOURCE CLASSIFICATION AND ORIGIN IDENTIFICATION USING GRID METHOD (KOJIMA, 2004)

For particle measurements, we selected a single grid square (5 x 5µm^2) from a SEM grid of each sample.
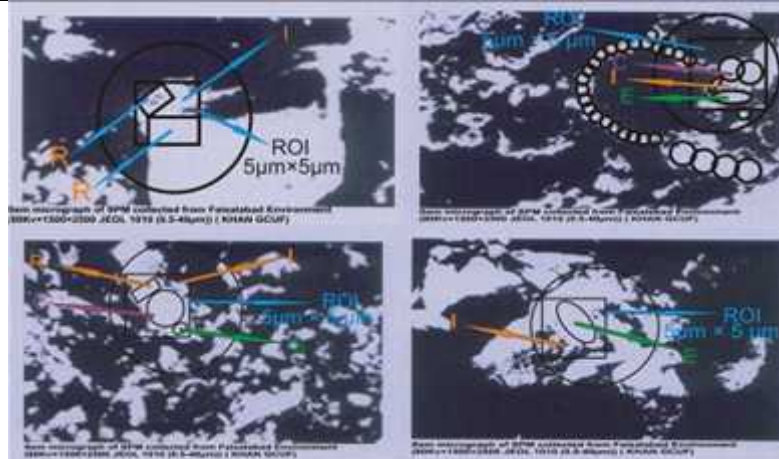
Fig. 1: Some SEM Micrographs showing Morphology of Solid Aerosols

Using the grid method, we found that the efficiency of this method is more than 90% as confirmed by XRD results [19-21].

3.2 SIZE DISTRIBUTION AND FINE TO COARSE RATIO

Size of particles identified ranges from 2µm to 93.33 µm comprising of both fine and coarse particles. The percentage of coarse particles was found to be 33.39% and that of fine particles was 66.61%. Hence giving fine to coarse ratio 1.995.which shows luminosity is less while opacity is more giving rise to number of accidents. Overall values for fine to coarse particles ratio with an average of 2.66 is given in table below:

Table 2: Mixing ratio of fine to coarse Solid Aerosols

Sample Code	pm2.5/pm10
2K01	2.608696
2K02	0.368421
2K03	2.529412
2K04	0.5
2K05	3.678571
2K06	8.5
2K07	2.615385
2K08	1.366667
2K09	1.772727
Average	2.659986

Which may be mainly due to human activities which includes industries and transportation in the area under investigation (10, main industries, 10 intercity highways, 15 intercity roads, (5 X 5) Km^2 grid). Industrial and Transportational derived aerosols fall in this range. Such particles remain suspended in the environment for a long time because they are not efficient nuclei of ice. These particles are inhalable and could cause serious health hazards. The solid aerosols in the range >10 – 93.3 µm

were found to be 33.39 %, it may be due to anthropogenic activities and geological area setup. Greenery and high rain fall (175 mm/24 hours) also contribute in suppressing these soil derived aerosols.

3.3 PARTICLE CLASSIFICATION

Five different particle classes were distinguished based on morphological and chemical composition obtained with SEM and XRD. The detail is as follows:

1) Internally mixed soot particles (soot with coatings of organic matter (OM), sulfates, or both; can be referred to mixtures of organic matter and sulfates as S   OM);

2) Soot particles without coatings (externally mixed soot OM   S);

3) Without soot (OM);

4) Tar balls;

5) Others

Samplewise enrichment of different classes/categories are shown in table below:

Table 3: Sample wise enrichment of different elements/compounds

Sample #	Sample code/ Identified phases	Type of Enrichment	Wt. percentage of element/ compound	Wt.%age of subgroups (elements/ compounds)
1	2K01/Q	Iron (Fe)	56.05%	Iron Rich = 20%
2	2K02/Q	Aluminium (Al),Silicon (Si), Calcium (Ca)	84.601%	Al, Si, Ca rich = 40%
3	2K03/IL	Aluminium (Al),Silicon (Si), Calcium (Ca)	70.47%	K, S rich = 30%
4	2K04/IL	Aluminium (Al),Silicon (Si), Calcium (Ca)	47.58%	K, S, Fe (mixed) rich = 10%
5	2K05/IL	Potassium (K), Sulphur (S)	56.18%	Illite rich= 50%
6	2K06/IL	Potassium (K), Sulphur (S)	40.38%	Quartz rich = 40%
7	2K07/Q	Iron (Fe)	79.15%	Gypsum rich = 10%
8	2K08/G	Potassium (K), Sulphur (S)	52.42%	
9	2K09/IL	Potassium (K), Sulphur (S), Iron (Fe)	67.30%	
10	2K10/Q	Aluminium (Al),Silicon (Si), Calcium (Ca)	70.70%	

Mean weight percentages of all the major phases and trace elements identified in all the samples are given in Table 4 & 5.

Table 4: Statistical analysis of major identified phases

Sample coding	Nature of the zone	Phases identified	Max	Min	Mean	S.D.	CV
2K95	R/C	IL	64.21	6.15	35.18	41.05	116.68
2K14	R/C	CA	64.52	1.92	33.22	44.26	133.23
2K15	I/T	G/T	70.58	4.22	37.41	46.90	125.36
2K47	I/T	Q	64.02	8.68	36.35	39.13	107.64
2K32	R/C	CH/CL	40.41	6.11	23.26	24.25	104.25
2K42	I/T	AL	34.20	6.51	20.36	19.57	99.11

Table 5: Concentrations of Trace Elements (ppm)

Sample Coding	Nature of The Zone	Element Identified	Max. conc.	Min. conc.	Mean	SD	CV
2K16	R/T	Ni	0.90	0.001	0.4505	0.6357	141.12
2K78	T/R	Cu	2.12	0.001	1.0605	1.498	141.25
2K11	R/C	Pb	0.082	0.001	0.0415	0.057	27.14

In XRD studies and SEM micrograph analysis minor phases are not identified. Compounds and elements present in samples came from normal soil minerals, so origin of these samples is primary origin. Elements identified by AAS are indifferent from phases identified by XRD and SEM micrograph analysis. This state of affairs indicates that elements are present due to physic-chemical changes in the environment due to industry, transport and fuel consumption. All these three sources have been identified in source identification of SEM also which shows that sources identified are of secondary origin. Almost all the elements/ compounds were confirmed through wet chemical analysis as shown below.

Wet chemical analysis of a few specially selected samples was also carried out and given below in tabular form to check the co-relationship between identified trace elements by AAS and Phases of compound analysis by XRD but nothing was found common between them [19 - 28] (Table 6).

Table 6: Wet Chemical analysis of the solid aerosols

Oxide	Percent composition of Solid Aerosols
SiO_2	60.4800
Fe_2O_3	9.3000
TiO_2	9.3000
Al_2O_3	9.3000
CaO	7.8000
Na_2O	5.1600
K_2O	2.6666
Loss of Sample was observed	12.0200

On the basis of composition, size and shape (CSS) using available data, the true representative of solid aerosols are as follows in Table 7.

Table 7: Shape wise origin identification (An overview)

Particle Classifications	Wt., Percentage
Angular (S + R)	17.38%
Circular (c)	27.83%
Irregular (I)	49.32%
Spherical (S)	5.48%
Fibrous (regular + irregular) (R + I)	100%

In this study, the larger variations in the shapes of solid aerosols were observed with reference to the origin of the solid aerosols. So, it is proposed that shape distribution of solid aerosols may be used as valuable tool for describing the physico-chemical composition of solid aerosols.

In most of the samples identified phases occur as patches rather than single grain, so heterogeneity and aggregation of the Faisalabad environment is a dominating factor in our experimental findings. One possible explanation is the conversion of the sulphides of identified phases into a soluble hydrous sulphate via oxidation processes which is confirmed by the sulphate mineral as Gypsum detected in clay minerals by XRPD technique. The other possible explanation is that to produce aggregates. There must be some mechanism that groups particles to gather in to clusters and also some means by which they are firmly bound so that the structural form persists. Clay minerals, oxides of iron and manganese, and colloidal organic matter are important cementing materials. As colloidal particulate matter are charged bodies, dipole water molecules attach themselves firmly as water molecules also carry positive and negative charges due to evaporation of water molecules from particulate matter, length of each linkage becomes shorter and shorter, making cemented bonds stronger and stronger. Due to this conjunction aggregates are formed.

Another possible justification is the presence of fly ash, road dust and pollens in the Faisalabad environment which are synthesized by microorganisms already existing there. As a result suspended particulate matter gains positively and negatively charged groups. These groups interlock the identified phases into patches, the oval and irregular shapes of the majority of the samples also support our justification. (Confirmation of Presence of Fibrous Material). This state of affairs also confirms the stability of the Faisalabad environment.

The majority of Solid Aerosols contributing this study belongs to fine particle range and is of hydroscopic nature. They are acting as ideal absorbers and contributing a lot

in light extinction. This absorption of light activates the solid aerosols for physico-chemical reactions to take place and justify the secondary origin of solid aerosols in our findings. High relative humidity also supplements our results.

4.   CONCLUSIONS

Characterization and morphological structure study of solid aerosols related to Faisalabad environment has shown that most of the chemical composition comprises on the traffic, industry, local fuel combustion and dust re-suspension as indicated by source identification in our experimental findings elsewhere. On behalf of this study, we come at the following important conclusions:

- Size varies from 2µm to 93.33 µm and average fine to coarse ratio 2.66, much greater than that of other studies.
- Shape wise classification with their percentage was found to Angular (17.38%), circular (27.83%), irregular (49.32%), spherical (5.48%) and fibrous (regular + irregular) (100%).
- Five main classes, soot internally mixed, externally mixed with organic matter, pure soot, tar balls and others were identified showing the complexity of Faisalabad environment.
- The composition of the solid aerosols was found to be 20% Fe rich, 40% Al, Si, and Ca rich, 30% K and S rich, above 10% K, S, Fe mixed rich. Mixed primary and secondary origin confirmed through wet chemical analysis.
- Grid method shows almost similar results as that of other comparative studies which confirms the authenticity of Grid method.
- Colloidal nature of the most of particles due to oxidation and weathering process and synthesization of the solid aerosols due to microorganisms present in the environment.

The results of projects with further investigations will definitely improve the quality of our research work in estimating relevant parameters that define transport, distribution and interaction of pollutants from the sources of pollution to human population and are aimed for finding their effective solutions to improve the quality of the air and for a sustainable development in Faisalabad like other urban areas of the world. This is only possible if the special attention has to be paid on proper utilization of the experimental techniques within minimum possible errors, proper site selection, standard sampling techniques, data processing and data handling. However further work is suggested to reconcile satisfactorily the techniques used in this study and their co-relationship with Morphological structure studies.
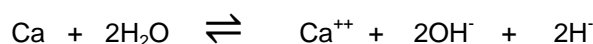
ACKNOWLEDGEMENTS

REFERENCES

1.   A. Chakraborty and T. Gupta, Aerosol and Air Quality Research, 10 (2010) 433.

2.   B. Dubey, A. K. Pal and G. Singh, India. Atmospheric Pollution Research, 3 (2012) 238.

3.   W. E. Failhing, Environ. Sci. Technol., 16 (1982) 237A.

4.   G. Gebre, Z. Feleke and E. Sahle-Demissie, Ethiopia. Bull. Chem. Soc. Ethiop., 24(3) (2010) 361.

5.   M. Z. Iqbal and M. A. Qadir, Radioanal, J. Nucl. Chem Letters, 144 (1990) 35.

6.   M. Z. Iqbal and M. A. Qadir, Int. J. Environ. Anal. Chem., 38 (1990) 533.

7.   M. Z. Iqbal and M. A. Qadir, Radioanal, J. Nucl. Chem. Letters, 145 (1990) 189.

8.   M. Z. Iqbal, M. A. Qadir and J. H. Zaidi, J. Trace Elem. Electrolytes Health Dis., 6 (1992) 63.

9.   M. A. Qadir, M. Z. Iqbal, and J. H. Zaidi, J Radioanal Nucl Chem. Lett., 166 (1992) 465.

10.   M. W. Ashiq, Z. Chuanyan, N. Jian and M. Akhtar, Theoretical and Applied Climatology. 99(3-4) (2010) 239.

11.   N. A. Kgabi, African Journal of Environmental Science and Technology, 4(11) (2010) 718.

12.   S. Ghan and S. E. Schwartz, Bulletin of the American Meteorological Society, 88 (2007) 1059.

13.   P. Khaenamkaew, P. Iamraksa, S. Raksawong, K. Wongsorndham and S. Khuntong, Journal of the Microscopy Society of Thailand, 24 (1) (2010) 37.

14.   R. Licbinsky, A. Frybort, J. Huzlík, V. Adamec, K. Effenberger, P. Mikuska, M. Vojtesek and K. Krumal, Transactions on Transport Sciences, 3(3) (2008) 137.

15.   G. Chesters, O. J. Attoe and, O. N. Allen, Soil Sci. Soc. Am. Proc., 21 (1957) 272.

16.   K. K. Shandilya and A. Kumar, Journal of Environmental Sciences, 22(2) (2010) 263.

17.   R. Garcia, M. C. Torres and A. Baez, Rev. Chemistry and Ecology, 24(2) (2008) 157.

18.   P. W. West and R. M. Pitombo, Anal Chem. Acta 37 (1967) 374.

19.   Y. Jamil, N. Amin, M. R. Ahmad, Z-ul, Haq and A. Hussain, Soil & Environ, 27(1) (2008) 84.

20.   J. H. Kroll and J. H. Seinfeld, Atmospheric Environment, 42 (16) (2008) 3593.

21.   T. Kojima, P. R. Buseck, Y. Iwasaka, A. Matsuki and D. Trochkine, Atmos. Res., 82 (2006) 698.

22.   A. Karakatsani, A. Analitis, D. Perifanou, G. Ayres, Harrison, M. Roy, A. Kotronarou, I. Kavouras, Juha and G. Pekkanen, Environ. Health, 11 (1) (2012) 75.

23.   K. S. Johnson, B. Zuberi, L. T. Molina, M. J. Molina, M. J. Iedema, J. P. Cowin, D. J. Gaspar, C. Wang and A. Laskin, Atmospheric Chemistry and Physics Discussions, 5 (2005) 5585.

24.   P. I. Jalava, R. O. Salonen, A. I. Halinen, P. Penttinen, A. S. Pennanen, M. Sillanpaa, E. Sandell, R. Hillamo and M. R. Hirvonen, Toxicology and Applied Pharmacology, 215 (2006) 341.

25.   R. M. Harrison, R. Perry, M. L. Jackson and G. D. Shareman, Hand Book of Air Pollution Analysis, 2nd Edition, Editors, Adv. Agronomy, 5 (1953) 219.

26.   R. K. Schofield, Jour. Soil Sci., 1 (1949) 1.

27.   S. P. Harrison, K. E. Kohfeld, C. Roelandt and T. Claquin, Earth-Science Reviews, 54 (2001) 43.

28.   H. Fu, M. Zhang, W. Li, J. Chen, L. Wang, X. Quan and W. Wang, Atmos. Chem. Phys. Discuss., 11 (2011) 20973.

ANNEXURE

Rocks and minerals or near equilibrium in the atmosphere adjust to the greatly reduce temperature and pressure in the environment this re adjustment or changes due to abnormal variation in temperature and pressure are called weathering, rusting of metals cracking of sidewalks and lost mortar between bricks are the few examples of weathering process major chemical weathering reactions due to abundance of water, oxygen and carbon dioxide accounts far hydration, oxidation and carbonation reaction. These reactions result distraction of existence mineral and synthesis new minerals. Sodium Chloride exits as the natural mineral halite. Sodium and Chlorine exist in the

crystals as ions that attract each other at the crystal faces the Sodium and Chlorine ions respectively attracts the negative and positive poles of water molecules. Adsorption of water molecules dislodges the sodium and Chlorine from the crystal and greatly increases their solubility, in this way mineral dissolved in water and is washed out, which accounts for the general absence of halite in the hummed regions, similar is the case with other missing minerals. There are two major groups of clay minerals, the Silicate clays which include Illite, Montmoriclonite, Vermiculite and Kaolinite and the Oxide clays which include primarily Iron and Aluminum oxides. The complexity of weathering system makes identification of their specific origins impossible. The nature of the weathering environment plays an important role in determining when a given mineral will be form. Illite formation is common in the temperature regions where weathering environment has not been intense. Alteration of Mica minerals by the partial loss of structural Potassium and hydration is common mode of Illite formation. Montmoriclonite formation requires an abundant supply of Magnesium and a neutral or only slightly acidic environment (PH value of most of the samples lies in alkaline phase). In the temperature regions Illite can change by alteration into Montmoriclonite.

$$Ca \ + \ 2H_2O \ \rightleftharpoons \ Ca^{++} + \ 2OH^- \ + \ 2H^-$$

$$Mg \ + \ 2H_2O \ \rightleftharpoons \ Mg^{++} + \ 2OH^- \ + \ 2H^-$$

$$K \ \ + \ H_2O \ \rightleftharpoons \ K^+ \ + \ OH^- \ + \ H^-$$

$$Na \ + \ H_2O \ \rightleftharpoons \ Na^{++} + \ OH^- \ + \ H^-$$

Adsorbed Phase   Solution Phase   Adsorbed Phase

PH X 24 =   187 - 0.3 (CEC) - percent H saturation

Table 7: Co-relationship between PH values, H and Base saturation

PH Value	H Saturation	Base Saturation
7	15 %	85 %
5.5	50 %	50 %
6 ------ 7	-------------	50 %

The table is developed using the above expression. Taking CEC approximate 13.

Hydrolysis of exchangeable bases as source of OH - for the soil solution (The exchangeable bases are hydrated, but have been shown to be not hydrated for simplicity of illustration).

EFFECT OF CARBON IONS EMITTED FROM PLASMA FOCUS ON TITANIUM SURFACE

A. HUSSNAIN[1]*, R. AHMAD[2], T. HUSSAIN[2], Z. A. UMAR[1], N. KHALID[1]
AND A. SAEED[3]

[1]Department of Physics, GC University, Lahore, Pakistan
[2]CASP, GC University, Lahore, Pakistan
[3]Gomal University, D. I. Khan, Pakistan
*E-mail address: ah.shah14@gmail.com

ABSTRACT: The energetic carbon ion beams originated from plasma column produced in Mather-type dense plasma focus (2.3kJ) is used for carburizing titanium substrate at room temperature, by increasing the carbon ion dose exposure. The titanium (Ti) samples are exposed at fix axial and angular position from the hollow copper anode tip. Surface properties of treated samples as a function of ion dose are studied for crystallinity, surface morphology and Micro-hardness using X-ray diffraction, scanning electron microscope, atomic force microscope and Microhardness tester. XRD results confirm the evolution of titanium carbide phases depending upon the substrate exposure to the carbon ion dose and angular position while smooth surface morphology is observed from SEM and AFM results while micro-hardness results of exposed samples showed significant improvement.

Keywords: Titanium carbide, dense plasma focus, surface modification, XRD, thin film.

1. INTRODUCTION

Titanium carbide is one of the most important transition metal carbides used as advanced ceramics. Hard TiC ceramics have a number of special properties of interest such as high hardness, melting point, excellent wear resistance and low friction coefficient [1-3] so used in various applications. The deposition of thin coatings of TiC has been achieved by many researchers using various techniques such as chemical vapour deposition (CVD) [4], cathodic arc plasma deposition [3], pulsed laser ablation [5], pulsed electrode surfacing [6] and some physical vapour deposition (PVD) techniques e.g. sputtering and ion implantation are other typical techniques to deposit carbide films [7-9]. Dense plasma focus (DPF) is one of the efficient PVD techniques. The novelty of plasma focus system is that the ion beams emerging from plasma focus is being successfully used as thin film deposition, ion implantation, change of phase in thin films, thermal surface treatment and surface modification of materials and alloys [10-13]. The dense plasma focus (DPF) is a pulsed coaxial plasma accelerator and a simple, cost effective device that utilizes the self-generated magnetic field to compress the plasma to very high densities ($\sim 10^{25}$–10^{26} m^{-3}) and temperatures (1–2 keV) [14]. The DPF devices operating from a few kJ to MJ of energy emit ions of characteristic energy from a few keV to a few MeV [15, 16], fusion neutrons, relativistic electrons, soft and hard X-rays. Bhuyan et. al. [17] estimated the maximum ion energy for H$^+$, C^{+4} and C^{+5} which was in the range of (200-400) keV, (400-600) keV and (900-1100) keV respectively, whereas maximum densities were

within the energy ranges (60-100) keV, (150-200) keV and (350-450) keV respectively. The energetic ion (carbon) streams emitted from plasma focus are used for the formation of thin film of titanium carbide onto the titanium surface that enhanced the surface properties. The samples are exposed to the various numbers of irradiated focus shots at 7 cm from the anode tip and at angular (0° and 10°) positions with respect to anode axis.

2.   EXPERIMENTAL SET-UP

In this present work, we have used the DPF device as a source of energetic carbon ion, for the carburizing of the titanium substrate. The ion beams are emitted preferably along anode axis, in the shape of a fountain, spreading outward with anisotropy in their angular distribution [18]. The schematic assembly of the DPF device used in this paper for the carburizing purpose is shown in Figure 1. The DPF system installed in PTL-GCUL is Mather-type focus, powered by a single capacitor (32 µF, 15 kV), which is discharged by a fast switching system. The electrode system of the DPF device consists of a copper anode encircled by six symmetrically placed copper rods as a cathode. The tip of copper anode is engraved 15 mm deep to reduce the contamination in plasma which minimizes the copper impurities [19]. An insulator sleeve of Pyrex glass material with effective length 25 mm is fitted in between the electrodes to support the low inductance breakdown. Further details of DPF device can be seen elsewhere [20]. The plasma chamber is evacuated up to 10^{-2} mbar by a rotary vane pump and methane gas is filled in DPF chamber. Tariq et. al. [21] investigated that the focusing efficiency of plasma focus increases with increase of working (nitrogen) gas pressure. The Ions energy and velocity also increases with the increase of working gas pressures. While the ions flux decreased with the increase in the working gas pressure. So focusing efficiency of plasma focus was monitored by varying the methane gas pressure. By this way optimum pressure was obtained and during each shot, the gas pressure was kept static at 2.5 mbar so as to have good focusing and after a few shots fresh gas was refilled.

Capacitor bank delivers electric energy to electrode assembly, discharge initiates and gas break down occurs across the insulator sleeve surface. The plasma current sheath detaches from the sleeve surface and is axially accelerated by the magnetic field (developed by electric energy which is delivered by capacitor to electrode assembly). After the current sheath reaches at the open end of the anode, a dense plasma column is formed, which is unstable due to the growth of (m = 0) instabilities that causes a local high electric field. So that after disruption of plasma column, the

electrons and ions accelerated towards the opposite sides. Electrons move towards the anode while highly energetic ions move towards the substrate material. A shutter is placed between the top of the anode and the substrate material to avoid the unfocused ions from hitting the substrate material. A sharp spike in the voltage probe signal on the oscilloscope indicates a good focusing. For better results the samples are treated with good focus shots.
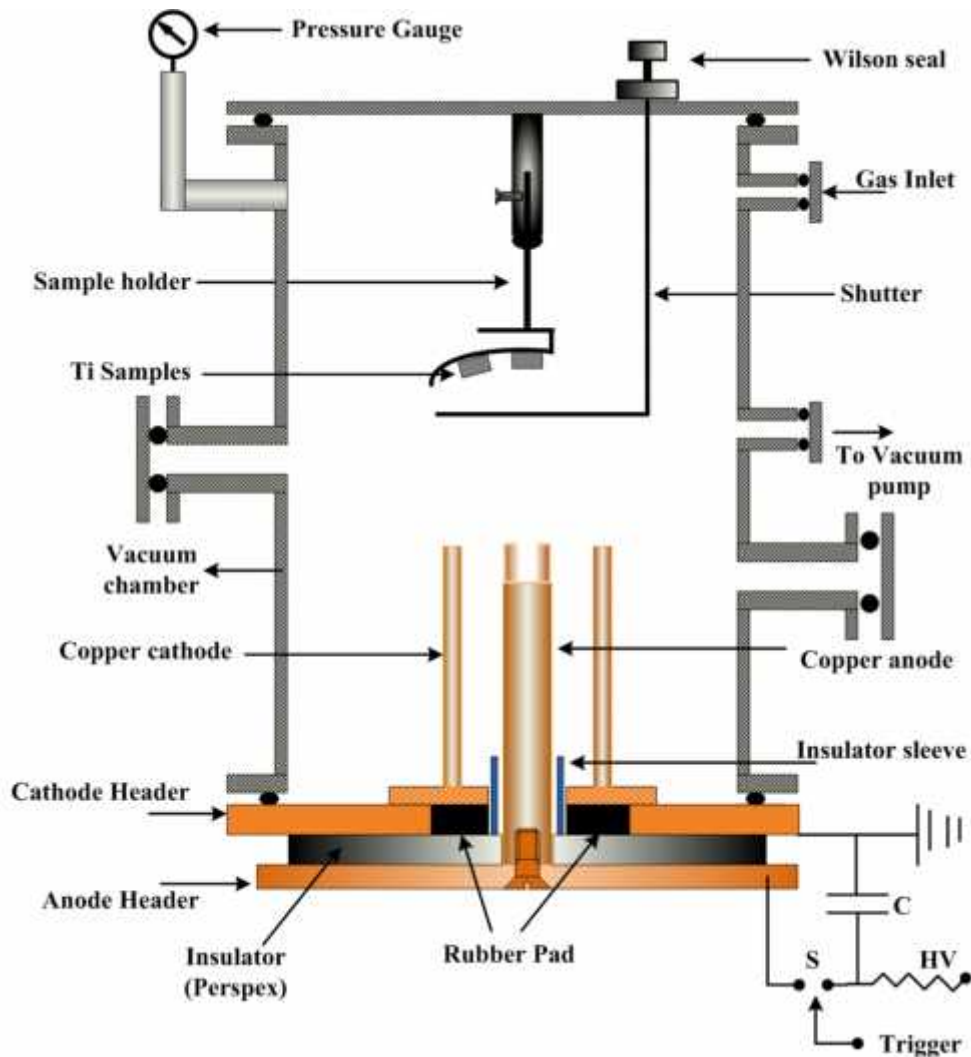
Fig. 1: Schematic of Experimental set up

Commercially available titanium samples of 9 mm × 9 mm dimensions were mechanically polished and then cleaned with ultrasonic water bath for 30 minutes and finally was washed with acetone before treatment. The samples were placed above the anode tip at 7 cm along anode axis, with the help of an axially moveable holder and were irradiated for different (5, 10, 20 and 25) numbers of focus shots Focusing was monitored on Tektronix (TDS 3054B, 500 MHz) digital storage oscilloscope using

a high voltage probe and a Rogowski coil to record the current waveform. A peak discharge current of 190 – 200 kA was observed.

The XRD analysis is carried out by using X'Pert PRO PANalytical MPD (–) scan mode using a CuK $_1$ (1.54 Å) radiation operated at 40 kV and 40mA. The surface morphology and roughness of the treated substrate was studied by scanning electron microscopy (SEM) and atomic force micrsoscopy (AFM) the surface hardness of substrate material was measured by a Vickers Microhardness tester.

3.   RESULTS AND DISCUSSION

3.1   XRD ANALYSIS

The XRD spectra of treated samples at $0^{°}$ and $10^{°}$ angular positions for 5, 10, 20 and 25 focus shots along with untreated sample is shown in the Figure 2 and Figure 3 respectively.

The XRD patterns at $0^{°}$ angular position demonstrate the evolution and restructuring of various phases of titanium carbide [TiC (111), TiC (222) and $Ti_2C_{0.06}$ (103)] at different number of focus shots. Various crystalline phases of deposited film with their plane reflections at ($0^{°}$ and $10^{°}$) are shown in Table 1. These XRD results are accordance with Inorganic Crystal Structure Database (ICSD).

Table 1: Various crystalline phases with their plane reflections

Angular Positions	Number of Shots	Various phases with their plane reflections			
		TiC		$Ti_2C_{0.06}$	
		Hkl	hkl	Hkl	Hkl
0 Degree	5	111	222	-	103
	10	111	222	-	103
	20	111	222	-	103
	25	111	222	-	103
10 Degree	5	111	222	101	103
	10	111	222	101	103
	20	111	222	101	103
	25	111	222	101	103

The XRD peaks of titanium carbide TiC (111), TiC (222), and $Ti_2C_{0.06}$ (103) appeared at 2 values of $35.4^{°}$, $76.6^{°}$, and $77.7^{°}$ respectively. Mechanism of forming different phases can be explained as follows: energetic ions having high flux beam cause melting and subsequent rapid cooling of the substrate surface [20], which results in re-crystallization and adsorption of the energetic species (like carbon ions) onto the

surface. As a result, new phases are formed during the molten state [21] and after the cooling some defects are developed within the bulk material [22]. The non-stoichiometric (metastable) $Ti_2C_{0.06}$ (103) phase developed due to the high surface free energy [23]. The titanium peak Ti (100) appeared at 35.2$^{°}$ position, for different number of focus shots (5, 10, 20, 25) shows slight decrease in the intensity while the broadening of the peak increases with higher number of focus shots, as consequence of carbon ions penetration ions increases the FWHM of the peak, which ultimately increases the hardness of the surface (will be explained later). A slight decrease in the intensity is observed in TiC (222) peak at 76.6$^{°}$ position.

The peak shifting of Ti (101) plane at two (0$^{°}$ and 10$^{°}$) angular positions for different number of focus shots is shown in the Table 2.

Table 2: Shifting of Ti (101) plane as a function of sample's angular position for the films deposited by different no. of focus shots

Sample angular position	Different peak positions of Ti (101) for different no. of focus shots				
	Untreated	5 Shots	10 Shots	20 Shots	25 Shots
0°	40.232	40.442	40.397	40.337	40.126
10°	40.232	40.389	40.402	40.252	40.192

For 0 degree case, at 5 shots the Ti (101) plane shifts towards higher angle due to the development of compressive stresses in the deposited film and decreases by increasing the number of shots. A similar behavior of compressive stresses in TiC (101) is observed at 10 degree case. The compressive stresses increase at 5 and 10 focus shots and then decrease at 20 and 25 shots. Compressive stresses are developed due to the incorporation of ions into the lattice sites, while the stresses are relaxed due to thermal shocks and resputtering.

The XRD spectra related to 10$^{°}$ position show that the peaks related to titanium carbide TiC (111), TiC (222), $Ti_2C_{0.06}$ (101) and $Ti_2C_{0.06}$ (103) are appeared at 35.4$^{°}$, 76.6$^{°}$, 43.2$^{°}$ and 77.6$^{°}$ positions respectively. Ti (100) phase appeared at 35.4$^{°}$ position shows some modification after exposure to the different number of focus shots. Due to the incorporation of the energetic carbon ions, FWHM of the peak increases while peak intensity slightly decreases. Ti (112) phase appeared at 76.45$^{°}$ shows slight broadening in the peak while peak intensity slightly decreases. TiC (222) peak is also appeared at higher number of focus shots (20 and 25). Non-stoichiometric $Ti_2C_{0.06}$

(101) phase is appeared at 43.2$^{°}$ at 5, 10, 20 and 25 shots while Ti$_2$C$_{0.06}$ (103) phase is appeared at 77.5$^{°}$.
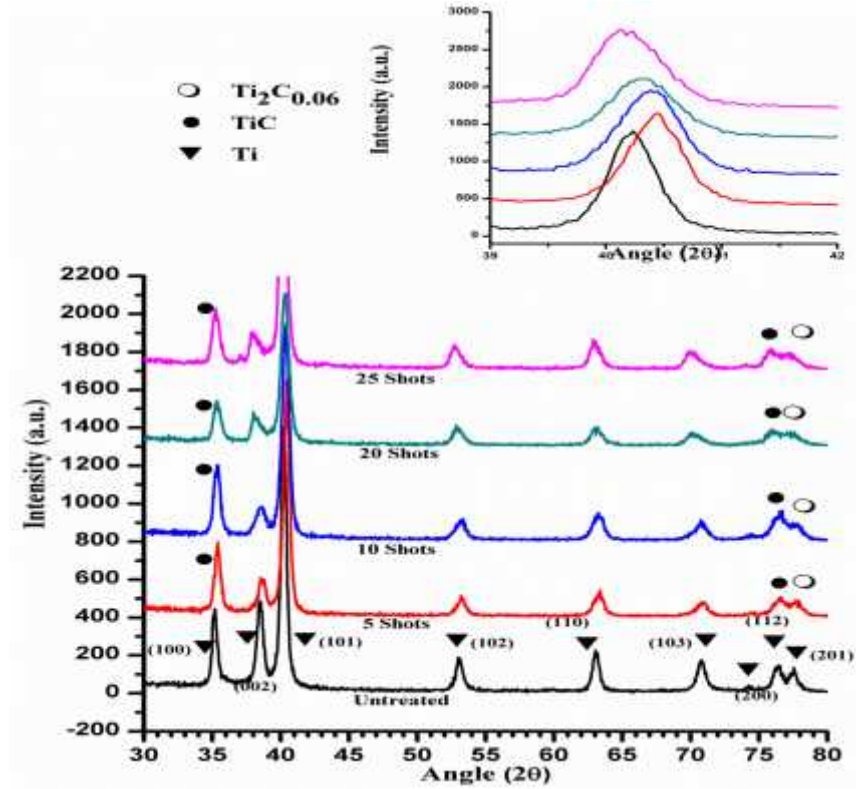

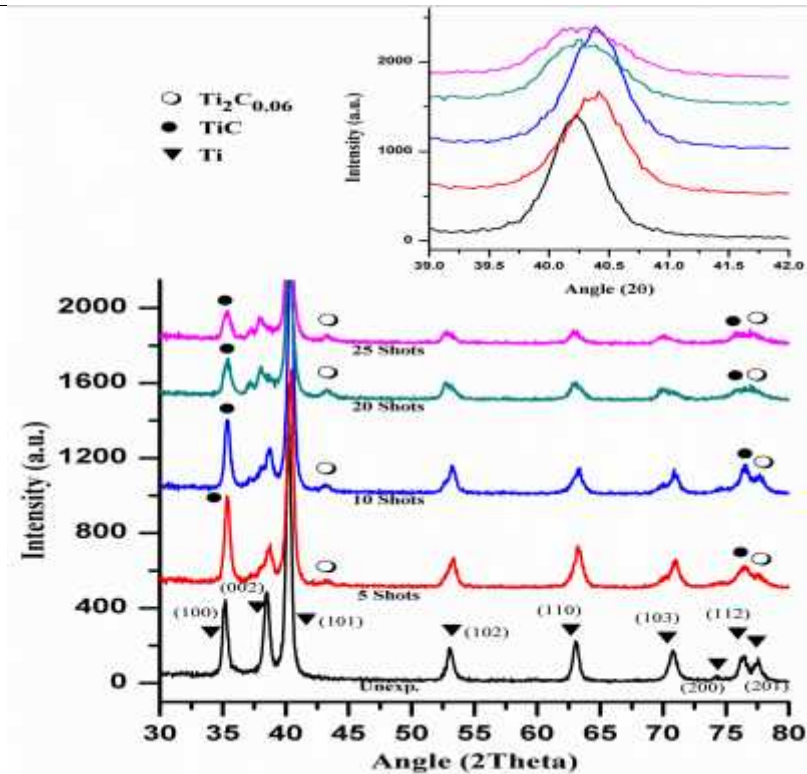Fig. 2: XRD spectra at 0 degree angular position

Fig. 3: XRD spectra at 10 degree angular position

3.2   CRYSTALLITE SIZE

The crystallite size is estimated from XRD data by using Scherers' formula [24].

$$Crystallite\ Size = \frac{k\}}{B\cos_{n}}$$

Where k = 0.93 is a Scherers' constant,   = 1.544 Å is the wavelength of the radiations,   is the Bragg's angle and *B* is the full width at half maxima (FWHM).

Figure 4 shows the variation in the crystallite size of TiC (111) peak at $0^{°}$ and $10^{°}$ with increasing the number of focus shots. For $0^{°}$ case the crystallite size after 5 shots decreases and remains almost same at 10, 20 and 25 shots. The decrease in crystallite size is probably due to the re-crystallization or incorporation of ions and the increase in the degree of deformation is also the cause of the decrease in the crystallite size [25]. The rise in the surface transient temperature and transfer of more energy to the substrate by increasing the number of focus shots (i.e. 25 shots) may be attributed with the re-crystallization of this phase.

For $10^{°}$ angular position, crystallinty of TiC (111) peak at 5 and 10 focus shots increases which is similar as observed in $0^{°}$ angular position, while the crystallinity increases at 20 and 25 focus shots.
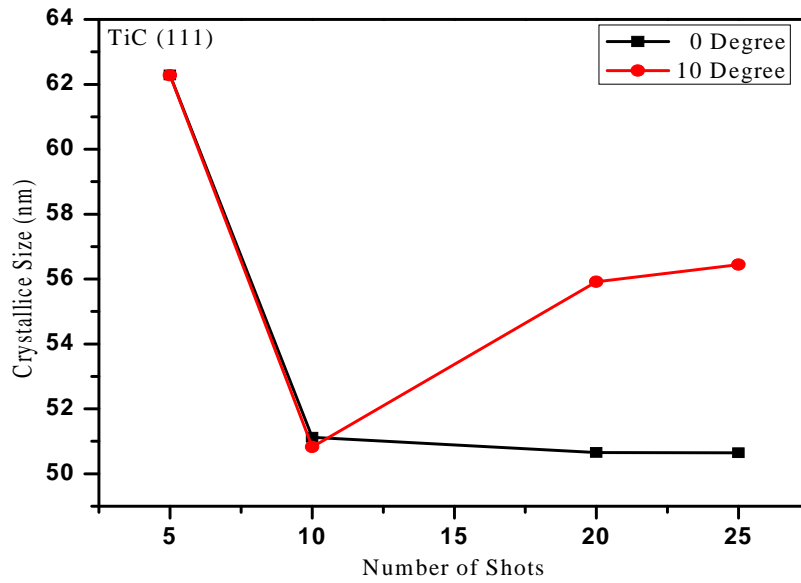
Fig. 4: Crystallite Size of TiC (111) phase

3.3   RESIDUAL STRESSES

Residual stresses in exposed and unexposed samples are determined by using XRD data. The ion implantation and thermal shock developed during the deposition process play an important role in producing compressive and tensile stresses in the deposited film. The stress due to ion implantation is generally compressive while the thermal shocks results in tensile stress [26].These stresses may also be confirmed from the up and down shifting of the diffraction peaks from their corresponding stress free data [27]. The peak shift may be due to the substitution of smaller or larger impurity (carbon/hydrogen) atoms. These residual stresses may also be attributed to the development of the lattice strains, which is due to the implantations of the impurity ions in the interstitial position, creation of the lattice defects and pulsed thermal shocks of the substrate surface. These strains can be calculated by using following formula [28].

$$\frac{\Delta d}{d} = \frac{d(Observed) - d(ICSD)}{d(ICSD)}$$

where $(\frac{\Delta d}{d})$ represents the strain in the crystalline surface. The residual stresses present in the deposited film can be calculated by multiplying the strain with the appropriate value of Young's modulus of the deposited film.

The Figure 5(a) shows the behavior of residual stresses developed in TiC (111) phase as a function of number of focus shots, at ($0°$ and $10°$) angular position from anode axis. For 5 focus shots at $0°$ position, tensile stresses are observed in the TiC (111).

The stresses decrease for 10 focus shots but slightly increase is observed for 20 and 25 numbers of shots. For 10° case at 5 shots tensile stresses are also observed in TiC (111) plane phase which are almost remained the same for 10 and 20 shots and then slightly increase a bit for 25 focus shots.
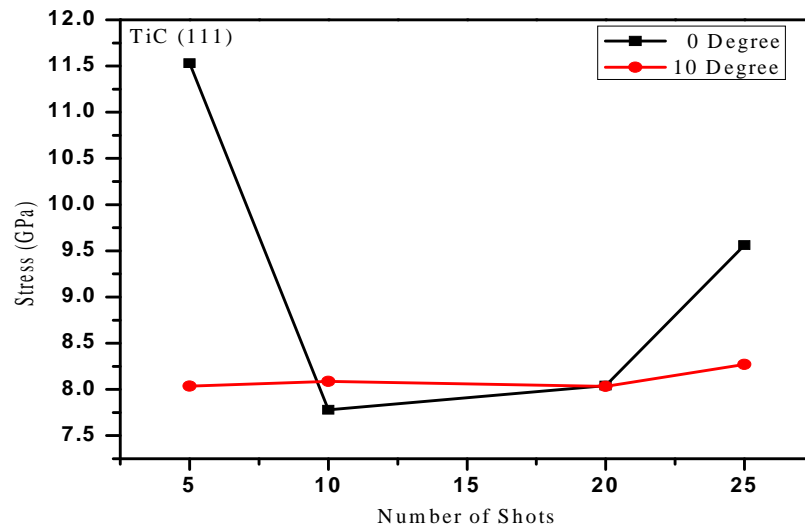

Fig. 5(a): Stress graph of TiC (111)

The Figure 5(b) shows the behavior of residual stresses developed for TiC (222) as a function of number of focus shots, and as the angular positions (0° and 10°) of the samples from the anode axis. For 5 focus shots at 0° position compressive stresses are observed in the TiC (222). Compressive stresses are decreased for increasing 10 focus shots while for 20 focus shots the compressive stresses completely changed into tensile stresses and tensile stresses are further increased for 25 focus shots. For 10° case (at 5 focus shots) compressive stresses are observed which decreases at 10 shots, while for 20 focus shots these compressive stresses also change into tensile stresses and tensile stresses are slightly decreased for 25 focus shots.
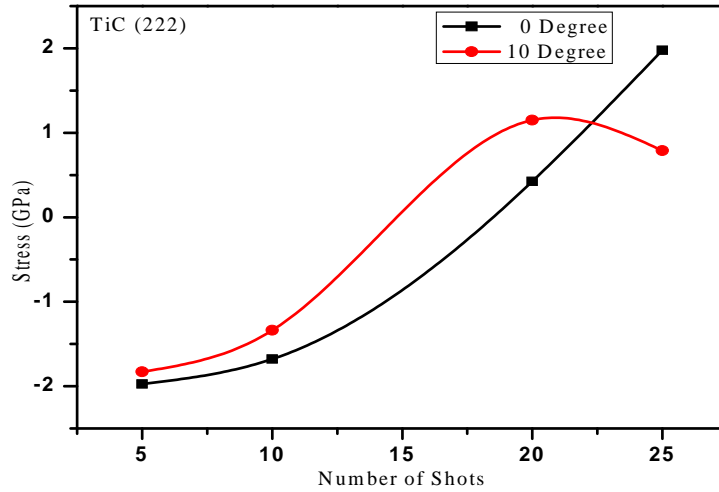
Fig. 5(b): Stress graph of TiC (222)

3.4.   SURFACE MORPHOLOGY

Figure 6(a) and Figure 6(b) shows the SEM results of the treated samples at $0^{°}$ and $10^{°}$ angular positions for 5, 10, 20 and 25 shots respectively along with untreated sample. Surface morphology clearly exhibits polishing marks on the untreated sample that developed during manual polishing process and almost been covered up by carburized surface. The DPF ion-assisted carburized thin film exhibits granular microstructure. The surface morphology of these carburized Ti-substrates is almost similar and exhibits the smooth thin film formation on the substrate surface.

The development of titanium carbide film on titanium substrate may be attributed to two different processes (a) direct implantation of energetic carbon ions into the titanium surface. These energetic ions may be incorporated interstitially into the titanium lattice and ions induced collision cascades creating point defects and distortion in its lattice structure [29] and (b) reaction of background carbon ions with evaporated titanium that may be redeposit onto the substrate surface [30]. Some cracks are observed in the deposited films at higher shots, which are may be due to thermal shocks developed during ion implantation or may be due to the mismatch between the lattice parameters of the deposited films and substrate.
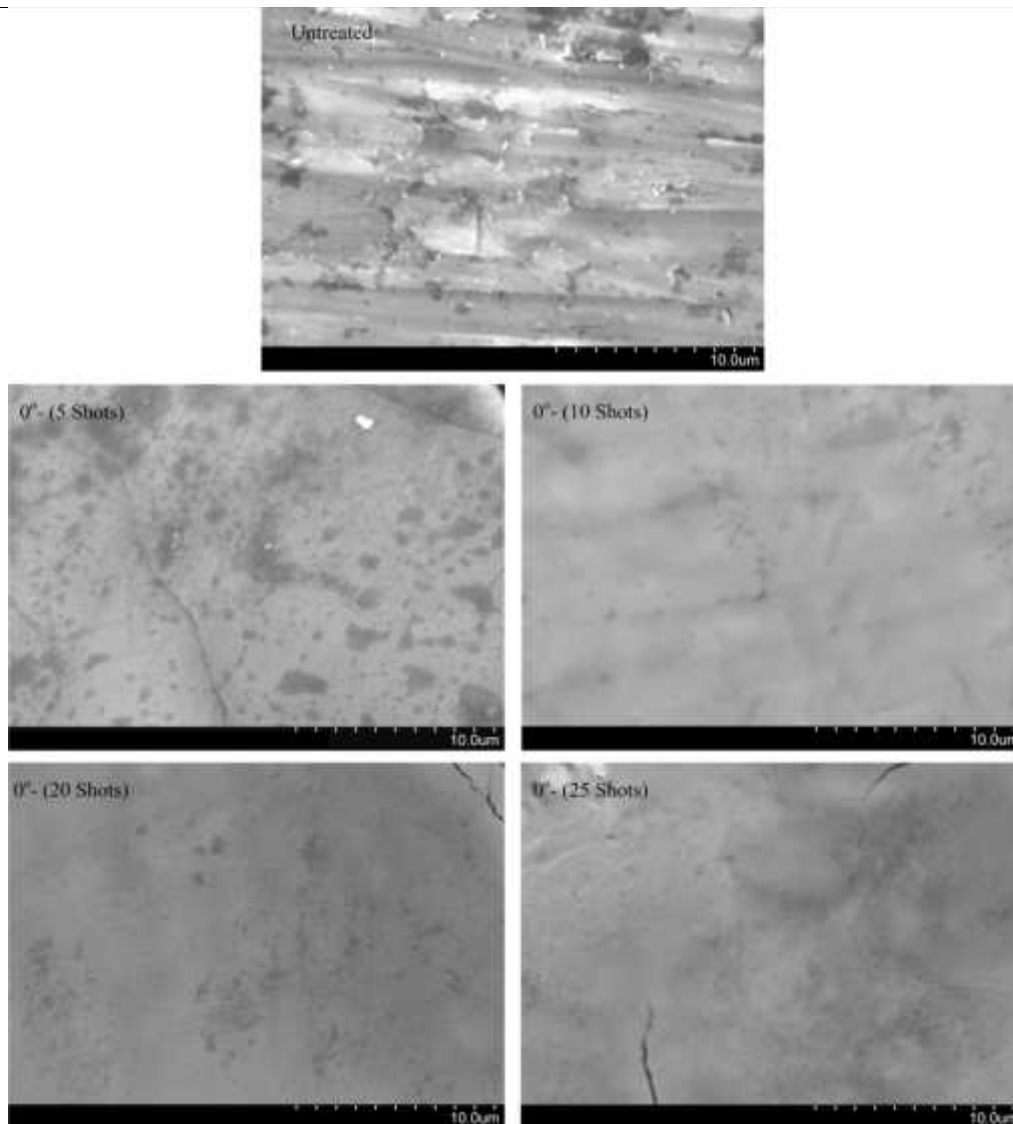
Fig. 6(a): SEM micro-graphs of untreated and treated samples at 0 degree angular position
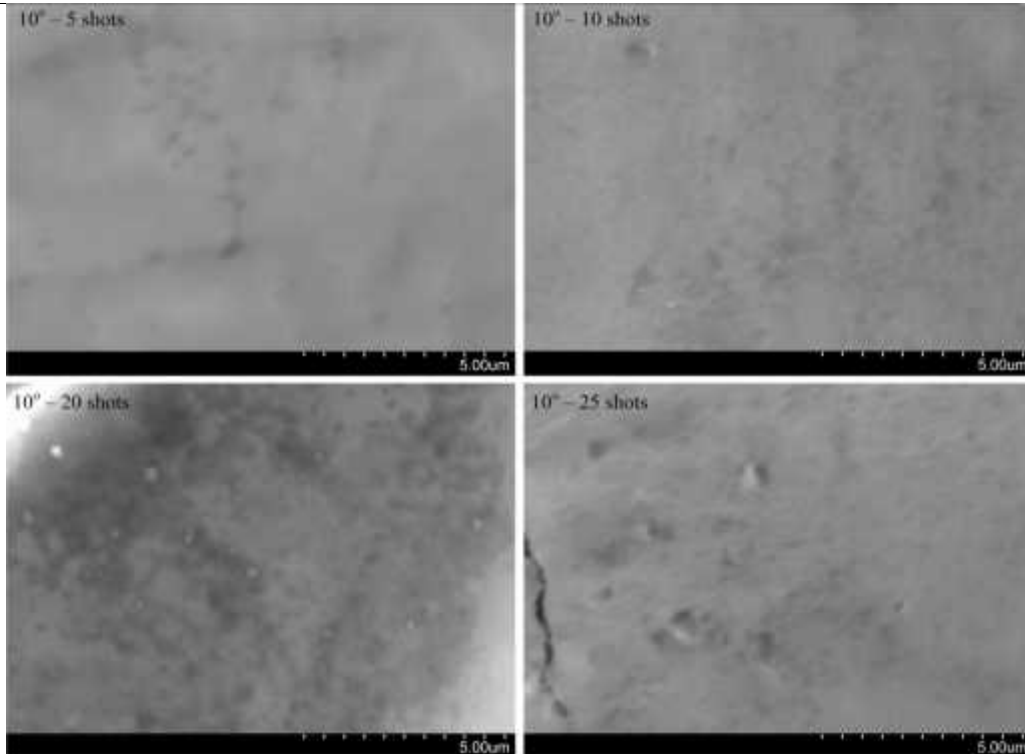
Fig. 6(b): SEM micro-graphs of treated samples at 10 degree angular position

Surface morphology of the carburized surface of the titanium was also analyzed using AFM. Figure 7 shows the surface topography and the RMS roughness of the untreated substrate surface and carburized titanium surface at different shots at 0° and 10° angular positions. The surface roughness of the treated samples is estimated from AFM images in terms of RMS value. It has been reported that in a single DPF focus shot, the emitted ions have a wide energy range with anisotropy in their angular distribution and considerably large number of ions were emitted in a small solid angle along anode axis and their flux decreases with the increase in the angle (18). These results predict the roughness would be different at different areas of samples, which is consistent with our results as shown in Figure 7. The surface topography of treated samples significantly improves and becomes smoother with increase in the number of shots and the RMS roughness values are observed as ~31 nm and ~24 nm at (0° and 10°) angular positions for 25 shots.
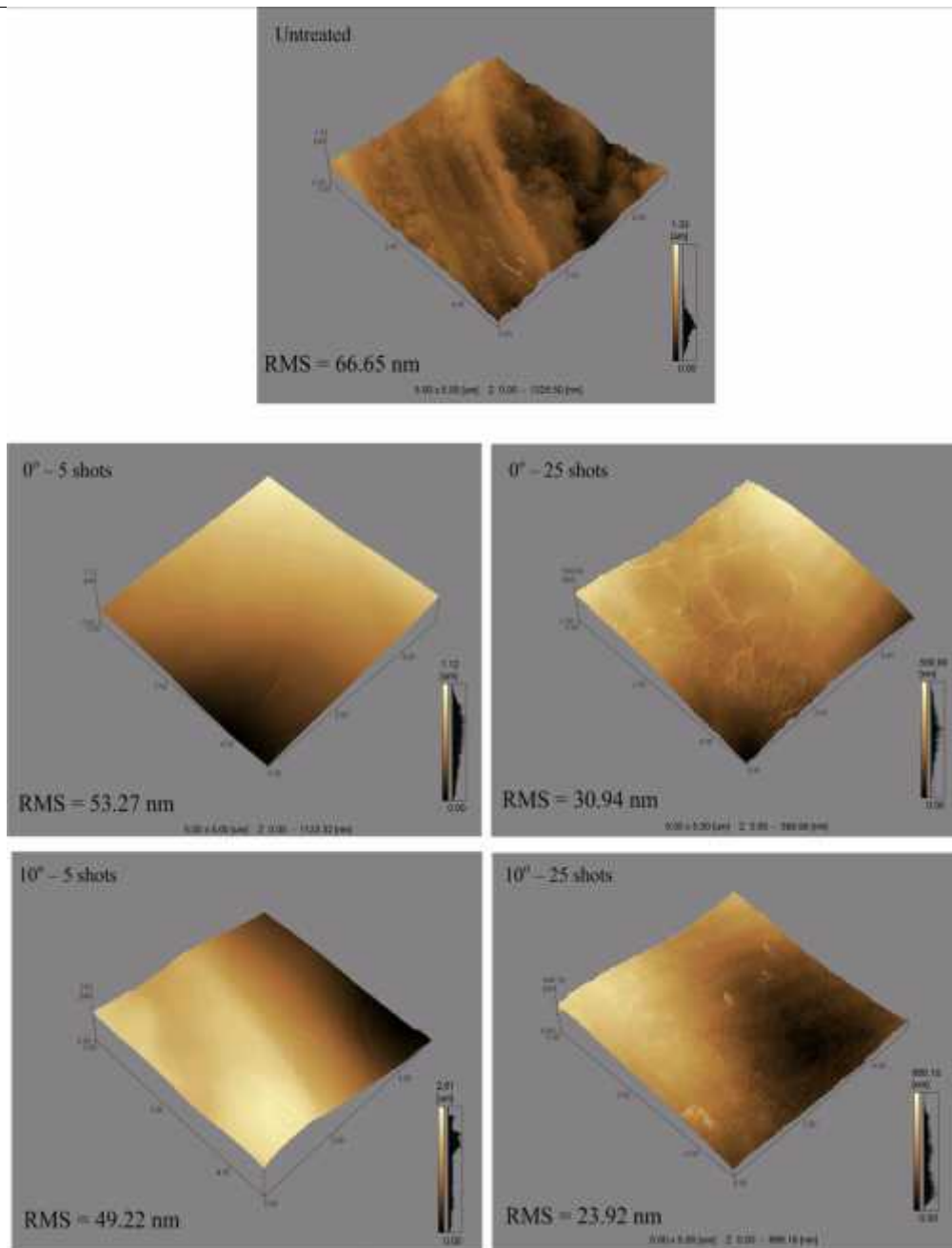
Fig. 7: AFM images of untreated, treated at 0 and 10 degree positions for 5 and 25 shots

3.5.   SURFACE MICRO-HARDNESS

A Wilson Wolpert 401 MVA Vickers micro hardness tester is used to measure the surface hardness of the carburized Ti substrates by applying various loads (10, 25, 50, 100 and 300 gf) for a dwell time of 10 seconds. Surface micro hardness (HV) of the treated samples at 0° and 10° angular positions from anode axis for 5, 10, 20 and 25 shots are shown in the Figure 8 and Figure 9 respectively. These microhardness

results of the treated samples are compared with the untreated one. The micro hardness profile represents significant increase in the micro-hardness of thin film formed on the titanium substrate, which may be due to ion implantation and formation of titanium carbide thin films. As the ion adsorption into the substrate is also the one of the cause of the increase in the microhardenss of the surface of Ti substrate.
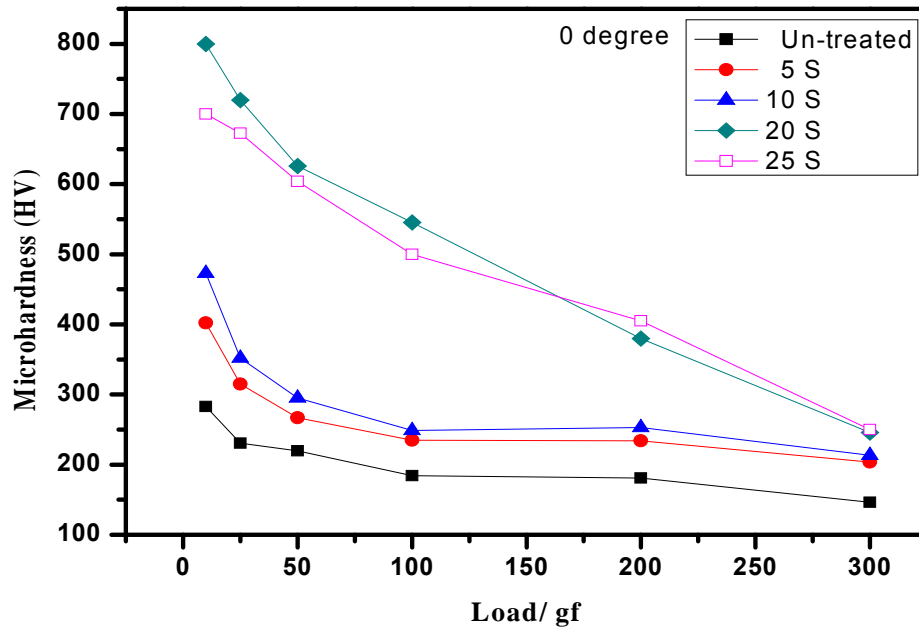

Fig. 8: Surface Micro-hardness graph at 0 degree

The microhardness graph at $0°$ position may be divided in two domains. Microhardness profile of the 5 and 10 shots are may be considered as first domain, showing a significant increase in the microhardness of the carburized Ti substrate. Microhardness profile of 20 and 25 shots may be consider as second domain, where maximum value of surface hardness is observed at 20 shots for 10 gf imposed load. The less decrease in the microhardness attributed to the formation of thick film of titanium carbide on the substrate. The microhardness graph at 10 degree represents the gradually increase in the microhardness value by increase in the DPF shots, while microhardness at 5 shots are higher than rest of the shots. At 5 shots microhardness 530 HV is observed at imposed load of 10 gf.
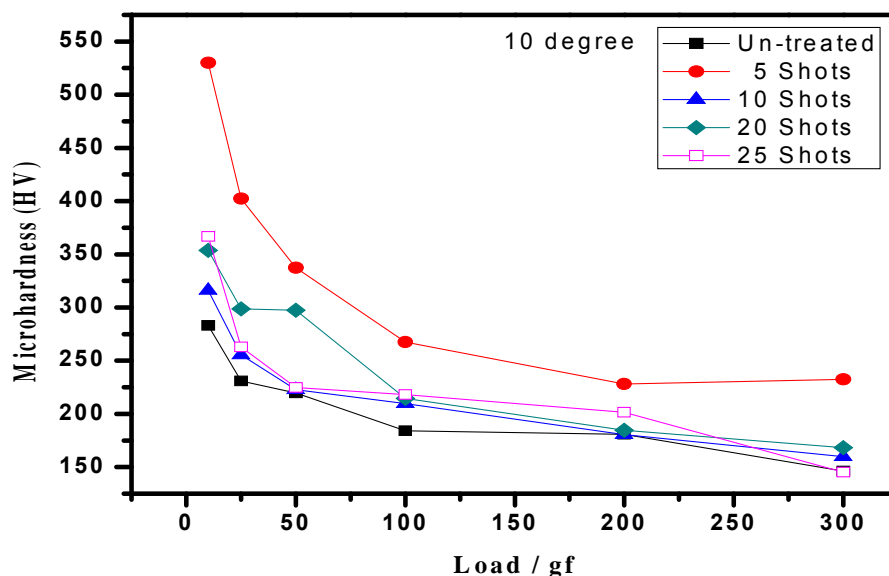
Fig. 9: Surface Micro-hardness graph at 10 degree

4. CONCLUSIONS

Titanium carbide films at room temperature are developed on the titanium substrate by using the energetic ion beams emitted from a plasma focus device. The XRD analysis revealed that the titanium carbide thin film is successfully deposited on the titanium substrate, which is also confirmed by the micro-hardness test results. The micro hardness measurements indicate reasonably hard titanium carbide film on the substrate. Various [TiC (111), TiC (222), $Ti_2C_{0.06}$ (101) and $Ti_2C_{0.06}$ (103)] phases of titanium carbide are observed. The XRD results show that the titanium carbide peaks are more intense at 10° as compare at 0°, while new phases of titanium carbide are observed at 10° position. The Vickers micro hardness profile indicates significant increase in the micro hardness of thin film formed on the titanium substrate. Smooth film with some cracks are observed using SEM.

ACKNOWLEDGEMENTS

REFERENCES

1.   T. Cho, D. G. Bat and P. F. Woerner, Surf. Coat. Technol. 29 (1986) 239.

2.   A. Derre, M. Ducarroir and F. Teyssandier, J. Electro. Chem. Soc. 136 (1989) 853.

3.   M. Pancielejko, W. Precht and A. Czyzniewski, Vacuum 53 (1999) 57.

4.   S. Eroglu and B. Gallons, J. Mater. Sci. 30 (1995) 1754.

5.   L. D. Alessio, A. M. Salvi, R. Teghil, V. Marotta, A. Santagata, B. Brunetti, D. Ferro and G. De Maria, Appl. Surf. Sci. 134 (1998) 53.

6.   A. Aggarwal and N. Dahotre, J. Mater. Eng. Perform. 8 (1999) 479.

7.   J. Tang, L. Feng and J. S. Zabinski, Surf. Coat. Technol. 99 (1998) 242.

8.   E. Kusano, A. Satoh, M. Kitagawa, H. Nanto and A. Kinbara, Thin Solid Films 343 (1999) 254.

9.   F. Alonso, J. J. Ugarte, D. Sansom, J. L. Viviente and J. I. Onate, Surf. Coat. Technol. 83 (1996) 301.

10.   S. R. Mohanty, N. K. Neog, B. B. Nayak, B. S. Acharya, P. Lee, T. L. Tan and R. S. Rawat, Nucl. Inst. Meth. Phys. Res. B 243 (2006) 113.

11.   M. Hassan, A. Qayyum, R. Ahmad, G. Murtaza and M. Zakaullah, J. Phys. D: Appl. Phys. 40 (2007) 769.

12.   R. S. Rawat, W. M. Chew, P. Lee, T. White and S. Lee, Surf. Coat. Technol. 173 (2003) 276.

13.   R. S. Rawat, P. Lee, T. White, L. Ying and S. Lee, Surf. Coat. Technol. 138 (2001) 159.

14.   S. Lee, T. Y. Tou, S. P. Moo, M. A. Eissa, A. V. Gholap, K. H. Kwek, S. Mulyodrono, A. J. Smith, Suryadi, W. Usada and M. Zakaullah, Am. J. Phys. 56 (1988) 62.

15.   H. Bhuyan, S. R. Mohanty, T. K. Borthakur and R. S. Rawat, Indian J. Pure Appl. Phys. 39 (2001) 698.

16.   H. Kelly, A. Lepone, A. Marquez, M. J. Sadowski, J. Baranowski and E. Scladnik-Sadowska, IEEE Trans. Plasma Sci. 26 (1998) 113.

17.   H. Bhuyan, H. Chuaqui, M. Favre, I. Mitchell and E. Wyndham, J. Phys. D: Appl. Phys. 38 (2005) 1164.

18.   L. Bertalot, H. Herold, U. Jager, A. Mozer, T. Oppenlander, M. Sadowski and H. Schmidt, Phys. Lett. A 79 (1980) 389.

19.   K. Takao, T. Honda, I. Kitamura and K. Masugata, Plasma Sources Sci. Technol. 12 (2003) 407.

20.   T. Hussain, R. Ahmad, N. Khalid, Z. A. Umar, A. Hussnain, Nucl. Instrum. and Methods. in Phys. Res. B 269 (2011) 1951.

21. H. A. R. Tariq, I. A. Khan, U. Ikhlaq and A. Hussnain, J. Nat. Sci. Maths., 48 1&2 (2008) 65.

22. G. Sanchez and J. Feugeas, J. Phys. D: Appl. Phys. 30 (1997) 927.

23. J. N. Feugeas, G. Sanchez, C. O. de Gonzalez, J. D. Hermida and G. Scordia, Rad. Eff. Defects in Solids, 128 (1994) 267.

24. K. Nordlund, M. Ghaly, R.S. Averback, M. Caturla, T. Diaz de la Rubia and Tarus, J. Phys. Rev. B 57 (1998) 7556.

25. M. Hassan, R. S. Rawat, P. Lee, S. M. Hassan, A. Qayyum, R. Ahmad, G. Murtaza and M. Zakaullah, Appl. Phys. A 90 (2008) 669.

26. B. D. Cullity and S. R. Stock, Elements of X-ray Diffraction, 3rd Ed., Prentice Hall, New-Jersey, 2001.

27. C. S. Chen, C. P. Liu, C. Y. A. Tsao, Thin Solid Films 479 (2005) 130.

28. V. N. Gurarie, P. H. Otsuka, D. N. Jamieson and S. Prawer, Nucl. Instrum. Methods Phys. Res. B 242 (2006) 421.

29. P. Tyagi and A.G. Vedeshwar, Phy. Rev. B 66 (2002) 075422.

30. R. S. Rawat, P. Arun, A. G. Vedeshwar, P. Lee and S. Lee, J. Appl. Phys. 95 (2004) 7725.

31. M. B. H. Breese, Mater. Res. Soc. Bull. 25 (2000) 11.

32. I. A. Khan, M. Hassan, R. Ahmad, A. Qayyum, G. Murtaza, M. Zakaullah and R. S. Rawat, Thin Solid Films 516 (2008) 8255.

SETTING UP OF A TOTAL INTERNAL REFLECTION FLUORESCENT MICROSCOPE (TIRFM) SYSTEM: A DETAILED OVERVIEW

A. R. KHAN[1]*, S. AKHLAQ[1], M. N. B. ABID[1], R. MUKHTAR[2], T. BUTT[1]
AND U. QAZI[1]

[1]Department of Life Sciences, SSE Biology, LUMS, Lahore, Pakistan
[2]Rahim Yar Khan College of Technology, Pakistan
*E-mail address: aaliya.rehman@gmail.com

ABSTRACT: The plasma membrane is the barrier which all molecules must cross to enter or exit the cell, and a large number of biological processes occur at or near the plasma membrane. These processes are difficult to image with traditional epifluorescence or confocal microscopy techniques since details near the cell surface are easily obscured by fluorescence that originates from the bulk of the cell. However, single molecule fluorescence techniques such as TIRFM have emerged as powerful tools to study biological processes at the cell membrane level. This article describes background, optical theory and hardware configurations used in setting up and application of TIRFM for characterization of kinetics of membrane adjacent cell processes. One such TIRF Microscope has been setup and made operational at the Department of Biology, School of Science and Engineering, LUMS, Pakistan since Oct. 2011.

1. BACKGROUND

Total Internal Reflection Fluorescence (TIRF) microscopy is quite a versatile imaging tool with high signal-to-noise ratio while at the same time eliminating maximum background noise [1]. TIRF utilizes the evanescent field created when a beam of light strikes an interface between two media to excite fluorescent dyes in the specimen. The phenomenon of total internal reflection occurs in which light is reflected but not refracted from a medium boundary and provides a means by which molecules close to the medium boundary can be imaged. Although TIRF cannot image deep into a specimen, it allows imaging of the specimen near the coverslip and/or the cell membrane adjacent phenomenon with high contrast compared to other techniques.

TIRF microscopy requires two optical media with different refractive indices, such as glass (n=1.51) and water (n=1.333). When a beam of light (laser in our case) hits an interface between the medium in which it is travelling and a medium of lower refractive index, part of the beam is refracted and part is reflected. The relative proportions of refracted and reflected light depend on the angle that the beam strikes the interface (termed the angle of incidence). The direction of propagation of the refracted wave, described by the angle θ', can be calculated by Snell's law:

$$n_1 sin\theta = n_2 sin\theta'$$

As the angle of incidence increases, the amount of light reflected also increases. Once the angle of incidence exceeds an angle known as the critical angle θ_c all light is reflected. This is known as total internal reflection.

$$\text{Sin}\theta_c = \frac{n_2}{n_1}$$

$$\theta_c = Sin^{-1}\left(\frac{n_2}{n_1}\right)$$

where θ_c is critical angle, n_1 is refractive index of first medium (e.g. glass) and n_2 is refractive index of second medium (e.g. water)
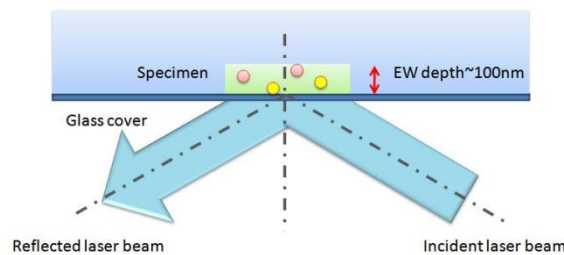

Fig. 1: Creation of an evanescent wave (EW) at the coverglass-specimen interface.

When light is totally internally reflected, some of the incident energy generates a very thin electromagnetic field that penetrates into second medium (Fig. 1). The intensity of this field decreases exponentially as it moves away from the interface and, as such, is called the evanescent field ('evanescent' meaning 'tending to vanish'). The evanescent field retains the frequency of the incident light and is capable of exciting fluorophores within approximately 100nm of the coverslip. The exact depth of penetration is dependent on the wavelength of the incident light and the angle of incidence. The depth of penetration decreases as the angle of incidence increases and as the wavelength of the light decreases. As the evanescent field only excites fluorophores within an exceptionally small distance of the coverslip, it gives a very thin optical section that eliminates background fluorescence.
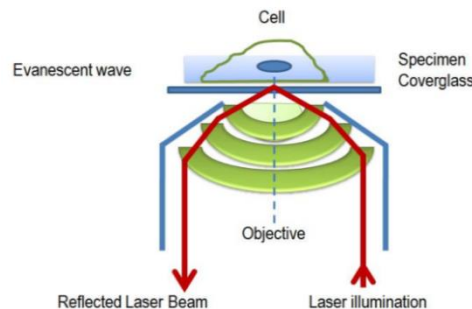

Fig. 2: Through-the-lens laser TIRF.

The development of high numerical aperture (NA) objectives has permitted total internal reflection using a through-the-lens approach. The NA of an optical system is a dimensionless number that characterizes the range of angles over which the system can accept or emit light (equation 1). The through-the-lens technique is more convenient, gives better spatial resolution and allows greater specimen accessibility. In this technique, the angle of illumination is varied by positioning the light beam off-axis at the back focal plane of the objective. The further off-axis the beam is positioned, the higher the angle of the incident beam and, therefore, the thinner the optical section. Illumination can be switched from TIRF to standard epifluorescence by repositioning the beam on-axis at the back focal plane (Fig. 2).

$$\theta_{max} = Sin^{-1}\left(\frac{NA}{n_{oil}}\right) \qquad (1)$$

where θ_{max} is maximum half angle of cone of emerging light beam that can enter or exit the lens, NA is numerical aperture of objective lens and n_{oil} is the refractive index of immersion oil. In the case of glass as medium 1 and water as medium 2 (n_1=1.52 and n_2 = 1.33), the critical angle is θ_c= 63°. If the incident angle θ is bigger than the critical angle, all of the wave's energy is internally reflected. For this case, the cosine of the outgoing angle becomes imaginary:

$$\cos(\theta') = \sqrt{1 - sin^2(\theta')}$$

$$= \sqrt{1 - \left(\frac{n_1^2}{n_2^2}\right) \cdot sin^2(\theta)}$$

$$= i\sqrt{\left(\frac{sin\theta}{sin\theta_c}\right)^2 - 1} \qquad (2)$$

The electric fields of incoming electromagnetic field $\vec{E}_1$ in the xy-plane and the generated outgoing electric field $\vec{E}_2$ at the time t and the position $\vec{r}$ can be described by the absolute amplitudes $\vec{E}_1^{\,0}$, $\vec{E}_2^{\,0}$, and their wave vectors $\vec{k}_1 = k_{1x}, 0, k_{1z}$ and $\vec{k}_2 = k_{2x}, 0, k_{2z}$:

$$\vec{E}_1 = \vec{E}_1^0 e^{i(\vec{k}_1\vec{r}-\omega t)} \qquad (3)$$

$$\vec{E}_2 = \vec{E}_2^0 e^{i(\vec{k}_2\vec{r}-\omega t)} \qquad (4)$$

For angles bigger than the critical angle, $\vec{E}_2$ can be expressed by equations (3) and (4) with the wave vector components (Fig.3.4) $\vec{k}_{2x} = k_2\sin(\acute{\theta})$ and $\vec{k}_{2z} = k_2\cos(\acute{\theta})$ as

$$\vec{E}_2 = \vec{E}_2^0 \cdot e^{i(\vec{k}_{2x}x + \vec{k}_{2z}zt - \omega t)}$$

$$= \vec{E}_2^0 \cdot e^{i(\vec{k}_2 x\left(\frac{n1}{n2}\right)\sin(\theta) - \omega t)} \cdot e^{\alpha z} \tag{5}$$

where the angle dependent parameter α is

$$\alpha = k_2 i \sqrt{\left(\frac{sin\theta}{sin\theta_c}\right)^2 - 1} \tag{6}$$

Even in the case of total internal refraction, the electric field in the second medium does not vanish due to the continuity of the Maxwell equations for interfaces of different refractive indices. The resulting electromagnetic wave is called an evanescent wave. The conundrum of a non-zero intensity in the second medium, while having total internal reflection, is solved by the fact that the time averaged energy flux density (described by the Poynting vector) [2] of the electromagnetic field vanishes. The evanescent wave enters the second medium, stays close to the surface and reenters the first medium again. The intensity of the evanescent wave as a function of the z-distance from the interface and the angle of incidence is given by the absolute value of the Poynting vector. The z-component of the intensity is given by equation;

$$I(z) = I_0 \cdot e^{-2\alpha z}$$

$$= I_0 \cdot e^{-\frac{z}{d_p}} \tag{7}$$

The field decays exponentially with the decaying constant d_p, which is called penetration depth.

$$d_p = \frac{n_2\lambda}{4\pi} i \sqrt{\left(\frac{sin\theta}{sin\theta_c}\right)^2 - 1} \tag{8}$$

It defines the distance from the interface where the intensity has decreased to approximately one-third of the original intensity I_0.

1.1   POINT SPREAD FUNCTION

The ideal point spread function (PSF) is the three-dimensional diffraction pattern of light emitted from an infinitely small point source in the specimen and transmitted to

the image plane through a high numerical aperture (NA) objective. It is considered to be the fundamental unit of an image in theoretical models of image formation. When light is emitted from such a point object, a fraction of it is collected by the objective and focused at a corresponding point in the image plane. However, the objective lens does not focus the emitted light to an infinitely small point in the image plane. Rather, light waves converge and interfere at the focal point to produce a diffraction pattern of concentric rings of light surrounding a central, bright disk, when viewed in the x-y plane. The radius of disk is determined by the NA, thus the resolving power of an objective lens can be evaluated by measuring the size of the Airy disk,

$$I(u) = \frac{1}{(1-\epsilon^2)^2} \left[\frac{2J_1(u)}{u} - \epsilon^2 \frac{2J_1(\epsilon u)}{\epsilon u} \right]^2 \qquad (9)$$

where *I(u)* is the surface brightness in the focal plane, normalized to its maximum at *u = 0, u* is a dimensionless distance from the optical axis in the focal plane and is related to the angular radius θ (as measured from the primary aperture) and the diameter *D* of the primary aperture as $u = \frac{\pi}{\lambda} D\theta$, ϵ is the fractional radius of the central obscuration of the primary aperture (assumed circular). The image of the diffraction pattern can be represented as an intensity distribution as shown in Fig. 3. The bright central portion of the Airy disk and concentric rings of light correspond to intensity peaks in the distribution. In this figure, relative intensity is plotted as a function of spatial position for PSFs from objectives having numerical apertures of 0.3 and 1.3. The full-width at half maximum (FWHM) is indicated for the lower NA objective along with the Rayleigh limit.
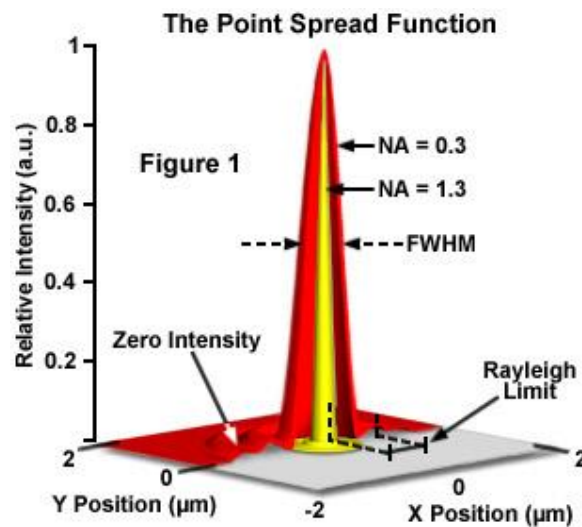

Fig. 3: The intensity distribution of the diffraction pattern [3]

In a perfect lens with no spherical aberration the diffraction pattern at the paraxial (perfect) focal point is both symmetrical and periodic in the lateral and axial planes. When viewed in either axial meridian (**x-y** or **y-z**) the diffraction image can have various shapes depending on the type of instrument used (i.e. widefield, confocal, or multiphoton) but is often hourglass or football-shaped. The point spread function is generated from the **z** series of optical sections and can be used to evaluate the axial resolution. As with lateral resolution, the minimum distance the diffraction images of two points can approach each other and still be resolved is the axial resolution limit. The image data are represented as an axial intensity distribution in which the minimum resolvable distance is defined as the first minimum of the distribution curve.

1.2   RESOLUTION LIMIT

The resolution limit of a light microscope is based on the wave structure of light. Passing through a light microscope, every incident light spot is spread through a certain region to the final projection area, as described by the point spread function. Two adjacent spots can be distinguished if the central maximum of the one point falls on the first tail maximum of the second point (Rayleigh-Criterion). The Abbe Limit originally developed by Ernst Abbe, describes this fact quantitatively. The limit states that a detail with a particular spacing in the specimen is resolved when the numerical aperture (NA) of the objective lens is large enough to capture the first-order diffraction pattern produced by the detail at the wavelength employed. The numerical aperture NA of a lens describes the lens's ability to collect or emit light and is defined as

$$NA \; = \; n \; \cdot \; sin\left(\frac{\alpha_{ap}}{2}\right)$$

with n being the refractive index of the medium in front of the lens and α_{ap} being the aperture angle of the lens. A common method to enlarge NA is the use of an oil immersion objective (Fig. 4a) instead of a dry objective (Fig. 4b). For these kinds of objectives, oil is placed between the lens and the glass slide of the sample, such that the refractive index matches that of the lens and the glass. The lateral resolution limit
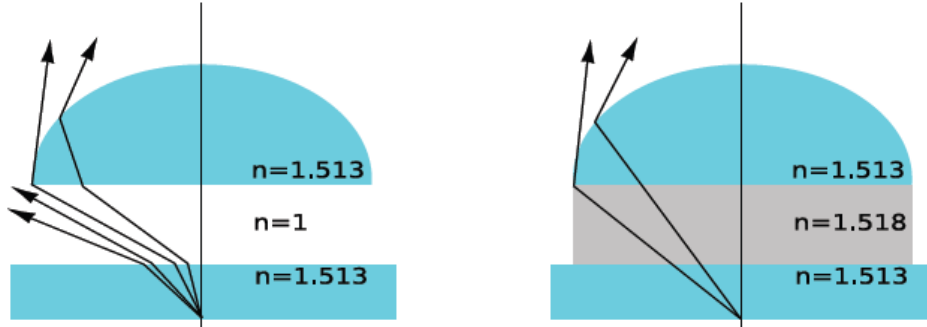
Fig. 4: (a) Dry setup with an air interface. The objective lacks the ability to collect big angles. (b) Matching the refractive index of the interface with immersion oil allows the use of a broader spectrum of angles, thus enhancing the resolution by increasing the numerical Aperture.

R_L^{lat} is given by

$$R_L^{lat} = 0.61 \cdot \frac{\lambda}{NA} \tag{10}$$

where λ is the wavelength of the light used. Accordingly, the axial resolution limit R_L^{ax} is

$$R_L^{ax} = \frac{2\lambda n}{NA^2} \tag{11}$$

According to Nyquist's sampling theorem [4] , lossless digitalization can only be achieved if the sampling rate is at least twice the maximum frequency response. Thus, at least two pixels are needed to recover the full information in the image and the observer (CCD camera or photoreceptor of the eye) reaches a lateral image resolution of *2 · pixel size*. The maximum possible magnification M is now the ratio of the observer resolution over the resolution limit given by the objective.

$$M = \frac{2 \cdot pixel\ size}{R_L^{ax}} \tag{12}$$

For this work an objective with a NA of 1.4 and a magnification of 60x as well as a laser with a wavelength of 488 nm is used. The results of these parameters are used in a maximum lateral resolution of 198 nm and a maximum axial resolution of 617 nm. The CCD camera has a pixel size of 6.45 µm, yielding a highest possible magnification of about M = 63.
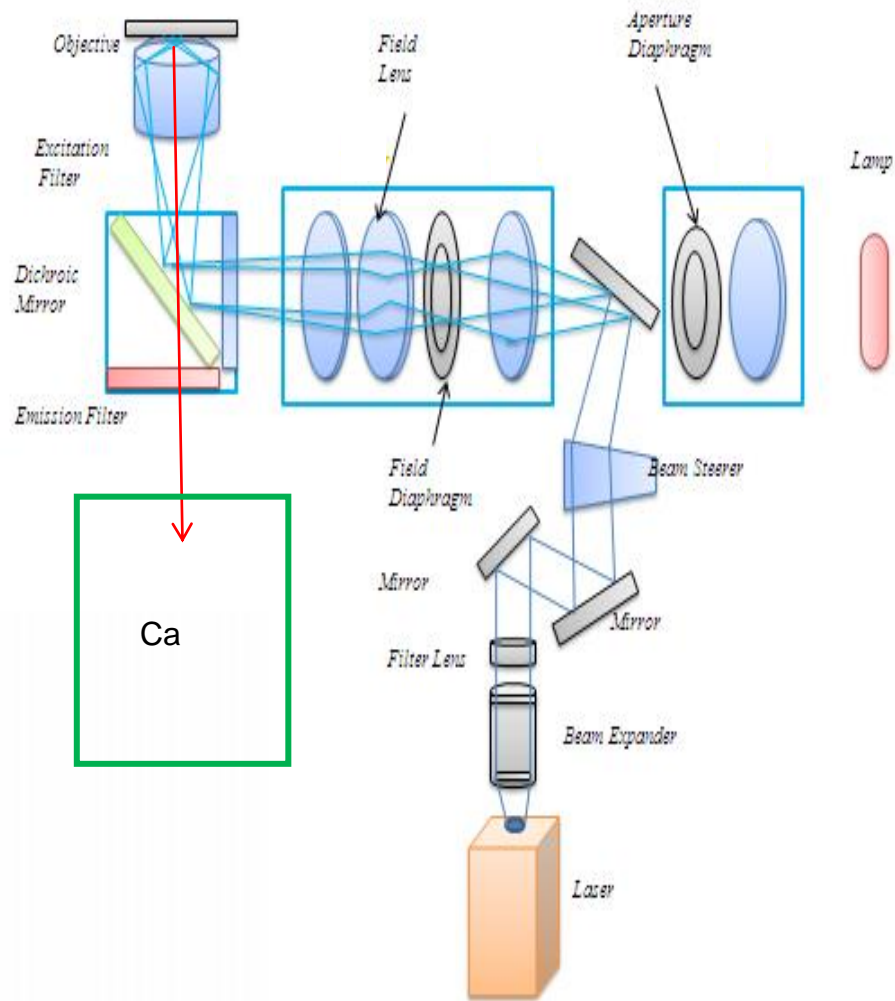
Optical Geometry

Fig. 5: The ray diagram preceding the experimental setup for TIRF measurements.

The laser used in our setup is Stradus™ 488nm diode laser with 50mW output and 200 MHz digital modulation (*Vortran Laser Technology, Inc,*) which served as illumination source for TIR illumination. The laser light is s-polarized and is coupled into the microscope by direct beaming. The laser housing contains a shutter device for fast switching of the laser illumination.

The objective used in this work is a 60× plan-apo objective with a numerical aperture of 1.4 (enhanced UV and IR correction from Olympus, USA). In this work the through-the-objective [5] is used which is based on the fact that off-axis laser light at the back focal plane of an objective leaves the objective lens under an angle. In order to gain only a narrow spread of angles, it is imperative to focus the laser beam in the back focal plane. The focus was set in this work by observing the spreading of the laser

beam at a high distance (i.e. ceiling of the room). The smallest possible spread of the beam gave the smallest possible spread of angles. With an approximate distance of d = 1.5 m between the objective and a smallest possible beam spreading of 3 cm, the angle can be set with an error of ±0.5%. This added to a total error in penetration depth, which can be found in Table1.

Table 1: Deviation of the penetration depth d_p for a variation of the angle of 0.5%

Angle	d_p	Deviation of d_p (%)
63°	158.1	13.9
65°	109.94	7.1
67°	91.8	3.5
70°	74.91	1.9

In order to reach angles big enough for TIRF microscopy, the highest possible angle has to exceed a threshold given by the critical angle which depends on the refractive indices of the immersion oil and the specimen. Given a refractive index of $n_2 = 1.518$ for the oil and a refractive index of approximately $n_1 = 1.33$ for the specimen (cell with medium), the critical angle is $\theta_C = 61.2^o$. The highest possible accessible angle is given by the numerical aperture of the objective. For a numerical aperture of NA = 1.4, the maximum angle is $\theta_{max} = 72^o$. TIRF images at angles close to θ_C will show illumination artifacts because inhomogeneities will convert some of the evanescent field into scattered propagating light (Fig. 5). The laser light was coupled to the optical path of the microscope directly via beam slider which introduced the laser light into the rear port of the microscope, normally used by the arc lamp. An equivalent back focal plane for the arc lamp existed in the rear part of the optical path where the arc lamp is normally imaged. This back focal plane was used to focus the laser beam. One advantage of a through-the-objective TIRF setup is the good accessibility of the sample. Furthermore it was possible to use TIR, epi and brightfield illumination in the same experiment. However, one big disadvantage of this method is that illumination is not only due to the evanescent field. A fraction of the illumination originates from scattering effects inside the objective and parts of the observed fluorescence intensity are due to luminescence of internal elements of the objective [6].

All TIRF measurements in this and later work are done with a Watec, WAT-902B monochrome camera (Industrial **Camera** Solutions from Aegis Electronic Group). The instant camera fulfills several prerequisites regarding pixel size, sensing area, sensitivity, low level of noise, and color depth. The size of the sensor pixels of the camera being small, spatial resolution is partially limited and highest possible magnification of the system is achieved. The combinations of pixel size of 8.4 µm×8.4

µm and NA as 1.4 lead to a highest possible magnification of 90x plus. The sensor area is the area given by the pixel size and the number of pixels. The number of pixels of the camera are 811(H)×508(V), or 0.41 mega pixel making the sensitivity of the camera a maximum in the range of 200 nm − 300 nm, which is the region of interest. The camera was connected to the microscope and a computer.
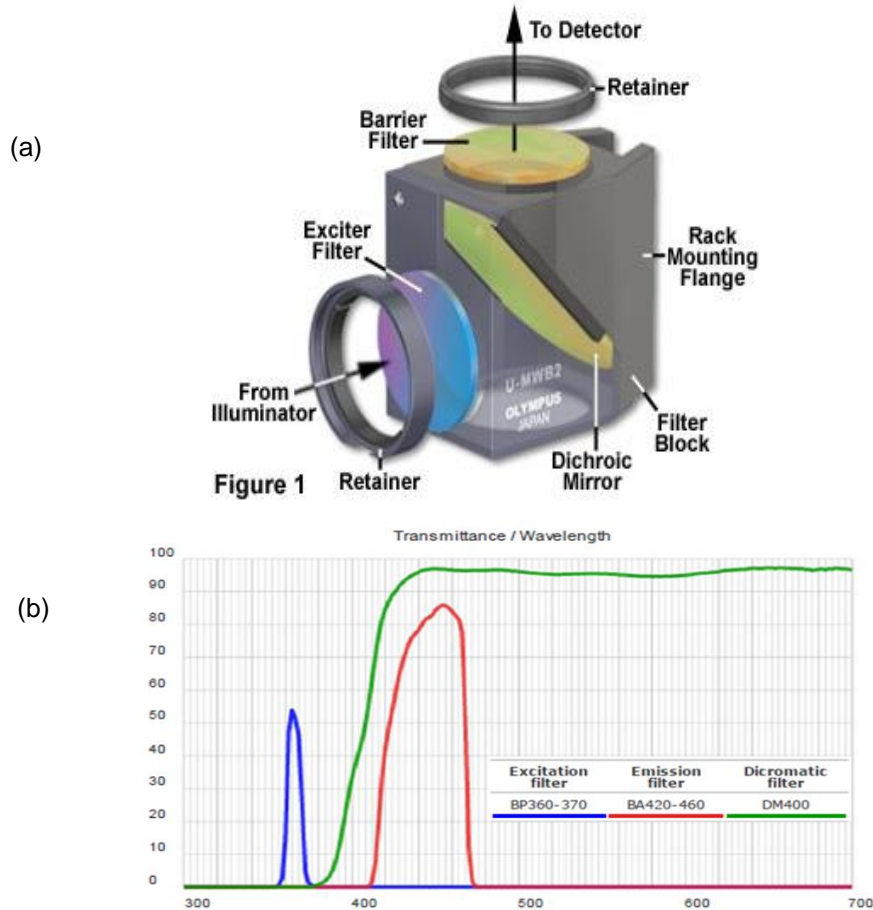
(a)

(b)

Fig. 6: (a) The fluorescent filter cube (U-MNUA2) and (b) the spectra for its 3 filters.

The Fluorescence Filter Cube used for our measurements is U-MNUA2 from Olympus [7] (Fig. 6a). Filter curves (spectra) show the percentage of transmission (or the logarithm of percentage) as the vertical axis and the wavelengths as the horizontal axis (Fig. 6b). The blue curve shows the spectrum of exciter filter which permit only selected wavelengths from the illuminator to pass through on the way toward the specimen. The letters **BP** associated with this filter stands for band pass, meaning that it is a filter with wavelength cut-off both to the left and to the right of its curve. Numbers associated with this filter (BP360-370) refer to the wavelength of maximum transmission for band pass exciter filters.

The green curve in Fig. 6b indicates the spectrum of Dichromatic beamsplitter (dichroic mirror) which is a specialized filter designed to efficiently reflect excitation wavelengths and pass emission wavelengths. These filters are always the interference type. Dichroic mirror is positioned in the light path after the exciter filter but before the barrier filter. It is oriented at a 45 degree angle to the light passing through the excitation filter and at a 45 degree angle to the barrier filter as illustrated in Fig. 6a. Abbreviations used to describe and identify beamsplitters DM for a dichroic mirror. The coatings are designed to have high reflectivity for shorter wavelengths and high transmission for longer wavelengths. They also have the additional functions of passing longer wavelength light to the barrier filter, and reflecting any scattered excitation light back in the direction of the lamphouse. The number DM400 indicates all the wavelengths above 400nm are allowed to move onwards to the Emission filter.

The red curve in Fig. 6b is for the Emission filter. The abbreviation BA denotes Barrier filter which blocks (suppress) shorter wavelengths and has high transmission for longer wavelengths. The number BA460 refers to the wavelength (in nanometers) at 50% of its maximum transmission. The red curve shows a sharp edge at the left side, indicating the blocking of wavelengths to the left of that edge [7].

3.   METHODS

For the measurements, silicate microspheres (PSi-10.0-OB, G.Kisker GbR, Germany) were put in a solution of glycerin (refractive index 1.37) and settled onto a glass coverslip. In order to keep sphere deformation due to drying low, the microspheres were readily introduced into the liquid. Approximately 10 minutes later the TIRF-measurements were performed to allow the spheres to sink down to the glass interface. The data analysis was performed using GMimPro, ImageJ and MATLAB. For the image analysis files were read into MATLAB in the tif format which stores images as two dimensional matrices, where a value is assigned to every (x,y) position in the image.

For the initial study, surface labeled silicate microspheres of diameter 10um and a low refractive index were used. Silicate microspheres have a refractive index of approximately 1.37, which can be matched by the help of the surrounding liquid in different ways [8]. Refractive index matching is an essential part of this measurement, because differences in refractive index between bead and medium create an effect called whispering gallery modes [9]. Whispering gallery modes are strongly confined, sustained electromagnetic modes inside dielectric spheres, which are generated by total internal reflection.
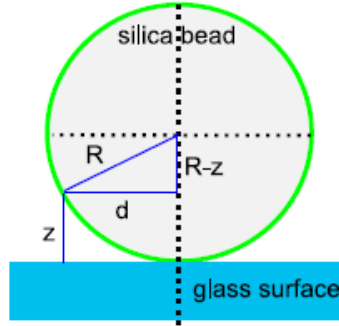
Fig. 7: Schematic drawing of the geometrical relations for a microsphere onto a glass interface.

The technique of directly visualizing the penetration depth with microspheres was first proposed by Mattheyses and Axelrod [6]. Large microspheres are settled onto a glass surface and the sphere's footprint is recorded. Because of the known geometry of the sphere (Fig. 7), a z-position can be assigned to every pixel in the xy-plane of the image. The z-position is given by the radius R and the lateral distance d from the center of the sphere

$$z = R - \sqrt{R^2 - d^2} \qquad (13)$$

Two corrections were necessarily, concerning the pixel size of the image and the curvature of the bead. The pixel character of the image leads to a displacement of the intensity information. This effect was be corrected, by assigning a radial bin to every pixel position (x−0.5, y−0.5), where x and y are the positions of the upper left corner of the pixel. Another implication of the pixel size is the effect it has on fluorescence emission from a curved surface. For pixels close to the center, the integrated intensity I' includes fewer z values than for pixels far away from the center. This effect was accounted for by the formula

$$I = I' \cos(sin^{-1}(\tfrac{d}{R})) \qquad (14)$$

We assigned a z-distance to every measured intensity and radius was measured using epifluorescence focused on the bead's equator.
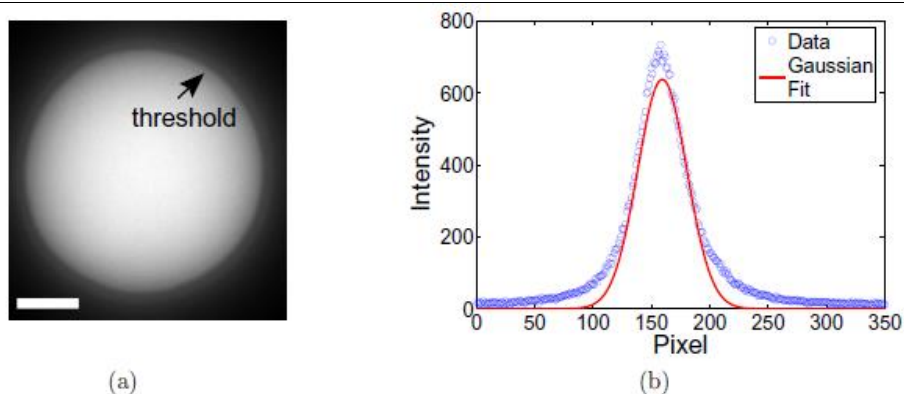
(a)

(b)

Fig. 8: (a) The radius of the sphere was measured by counting the amount of pixels exceeding a threshold value in epi-illumination (The bar in the figure is 2 µm). (b) The center of the sphere can be determined with a gaussian fit.

The number of pixels exceeding a threshold value, were counted, by which means the radius was calculated (Fig. 8a). The center of gravity was determined applying a gaussian fit to the data acquired under TIRF-illumination. For this purpose, the center was first approximated using the highest intensity in the image. A series of 10 gaussian fits in x and y direction around this center was used to find the actual center of gravity with an accuracy of ±1 pixel (Fig. 8b).
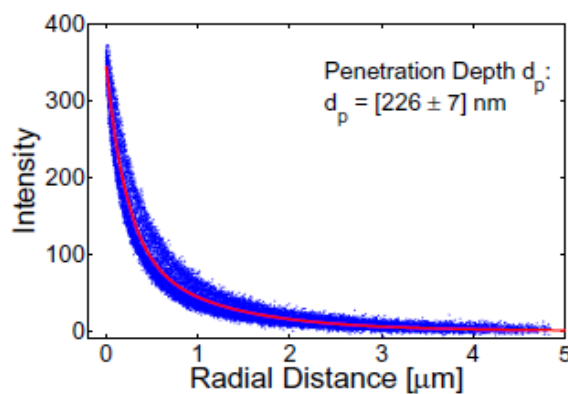

Fig. 9: Intensity values plotted over the distance from the interface show the decay of the evanescent field. The values were obtained using an angle of incidence of 67.3° and are part of a series of 20 different angles. A double exponential fit yields a penetration depth dp of 226 nm.

The intensity data was then plotted over the z-distance (Fig. 9). According to equation (7), an exponential fit to this data yields the penetration depth. A through-the-objective TIRF makes it necessary to include a second exponential function to compensate scattering effects [6].

4.   CONCLUSION

Once the TIRFM setup was completed, the operating system was verified by using 190nm diameter fluorescent microspheres in Brownian motion alternately in TRIF mode and brightfield mode of the microscope. The Figs. 10a and 10b show both respectively. One microsphere was stuck to the inner surface of flow cell and was taken as the standard illumination and then images were captured in both modes as the microspheres moved in and out randomly within the evanescent field. Figure shows one such scene where the microspheres are beyond the evanescent field and the area of interest is completely dark when viewed under TIRF conditions (apart from the stuck microsphere) while the same area when viewed in brightfield conditions shows further illumination coming from microspheres beyond the 200nm.
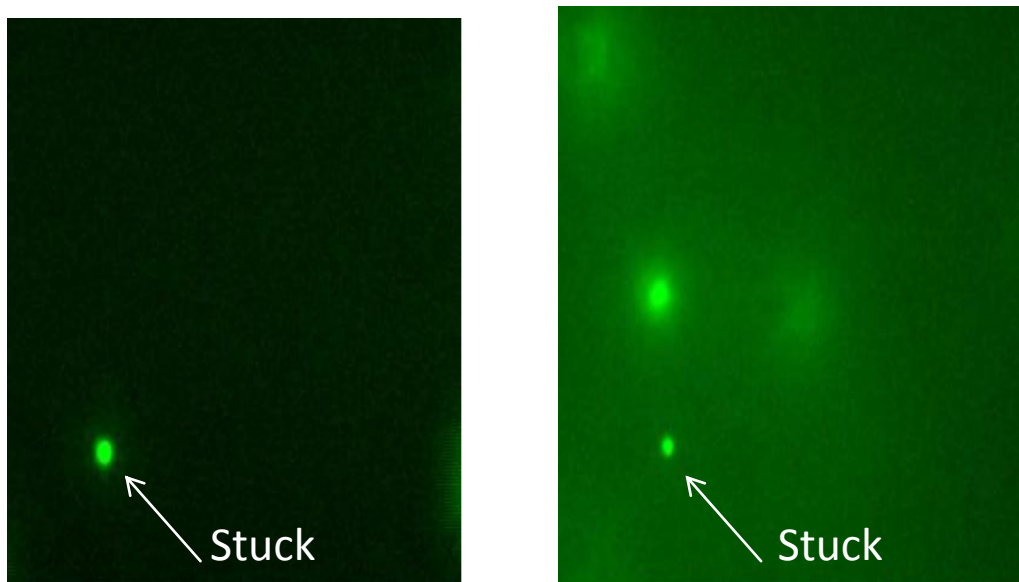

Fig. 10: Fluorescent microspheres viewed in TIRF and Brightfield modes of the microscope.

After the confirmation was made that the TIRFM setup was complete and consistent with the literature, we opened the lab in October 2011 for further study of real-time study of live cells and the processes adjacent to their membranes.

REFERENCES

1.   D. Axelrod, Traffic, 2(11) (2001) 764.
2.   J. H. Poynting, Phil. Trans. R. Soc. Lond. 175 (1884) 343.
3.   http://zeisscampus.magnet.fsu.edu.

4.   H. Nyquist, Trans. Am. Inst. Elect. Engs., 47(2) (1928) 617.

5.   A. L. Stout and D. Axelrod, Appl. Opt., 28(24), (1989) 5237.

6.   A. L. Mattheyses and D. Axelrod, J. Biomed. Opt. 11(1), (2006) 014006.

7.   http://www.olympusmicro.com/primer/techniques/fluorescence/filters.html

8.   B. P. Olveczky, N. Periasamy and A. S. Verkman, Biophys. J. 73(5) (1997) 2836.

9.   A. B. Matsko and V. S. Ilchenko, IEEE J. Sel. Topics Quan. Elect. 12(1) (2006) 3.